

1 **Toward a versatile spaceborne architecture for immediate**
2 **monitoring of the global methane pledge**

3 Yuchen Wang¹, Xvli Guo¹, Yajie Huo¹, Mengying Li², Yuqing Pan^{1*}, Shaocai Yu^{2*}, Alexander
4 Baklanov³, Daniel Rosenfeld⁴, John H. Seinfeld⁵, and Pengfei Li^{1*}

5
6 ¹College of Science and Technology, Hebei Agricultural University, Baoding, Hebei 071000, P.R. China

7 ²Research Center for Air Pollution and Health; Key Laboratory of Environmental Remediation and Ecological Health,
8 Ministry of Education, College of Environment and Resource Sciences, Zhejiang University, Hangzhou, Zhejiang 310058,
9 P.R. China

10 ³Science and Innovation Department, World Meteorological Organization (WMO), Geneva, Switzerland

11 ⁴Institute of Earth Science, The Hebrew University of Jerusalem, Jerusalem, Israel

12 ⁵Division of Chemistry and Chemical Engineering, California Institute of Technology, Pasadena, CA 91125, USA

13

14 *Correspondence to: Pengfei Li (lpf_zju@163.com)

15 Shaocai Yu (shaocaiyu@zju.edu.cn)

16 Yuqing Pan (panyuqing@hebau.edu.cn)

17

18

19

20

21

22

23

24

25

26

27

28

29

30

Submitted to

Atmospheric Chemistry and Physics

31 **Abstract.**

32 The global methane pledge paves a fresh, critical way toward Carbon Neutrality. However, it remains largely invisible and
33 highly controversial due to the fact that planet-scale and plant-level methane retrievals have rarely been coordinated. This has
34 never been more essential within a narrow window to reach the Paris target. Here we present a two-tiered spaceborne
35 architecture to address this issue. Using this framework, we patrol the world, like the United States, China, the Middle East,
36 and North Africa, and simultaneously uncover methane-abundant regions and plumes. These include new super-emitters,
37 potential leakages, and unprecedented multiple plumes in a single source. More importantly, this framework is shown to
38 challenge official emission reports that possibly mislead estimates from global, regional, to site scales, particularly by missing
39 super-emitters. Our results show that, in principle, the above framework can be extended to be multi-tiered by adding upcoming
40 stereoscopic measurements and suitable artificial intelligence, thus versatile for immediate and future monitoring of the global
41 methane pledge.

42 **1. Introduction**

43 Global methane pledges finalized at the COP26 (the 26th United Nations Climate Change Conference of the Parties) have
44 been never more ambitious (Schellnhuber et al., 2016; Schurer et al., 2018; United Nations, 2021). More than 100 countries
45 have promised 30% methane emission reductions by 2030. Also, energy giants (e.g., Shell and BP) have committed to clear
46 targets of methane mitigation. Such pledges have never been more essential within a narrow window (< ten years) to reach the
47 Paris target. The scientific context is that atmospheric methane is a powerful greenhouse gas second only to carbon dioxide
48 (CO_2), trapping ~ 80 times more heat than the same amount of CO_2 (per molecule) over a 20-year time horizon (Etminan et
49 al., 2016; Saunio et al., 2016, 2020). Worse still, it is thought to rise since 2007 (Mikaloff and Hinrich, 2019), surge since
50 2014 (Nisbet et al., 2019), and set another record in 2021 (National Oceanic and Atmospheric Administration, 2022).
51 Fortunately, methane is short-lived (\sim ten years) (Shoemaker et al., 2013), and, particularly, that from human activities can be
52 reduced in half using existing technologies by 2030 (Ocko et al., 2021).

53 However, a classic dilemma emerges, dimming the hopes of scientists and policymakers (Masood and Tollefson, 2021). That
54 is, on the eve of the Paris target, those targets and emissions remain largely invisible worldwide and thus hinder effective
55 mitigation. The main issue is the Paris framework relies on countries or corporate giants to report emissions (Allen et al., 2015;
56 Alvarez, Ramón A. and Zavala-Araiza, Daniel and Lyon, David R. and Allen, David T. and Barkley, Zachary R. and Brandt,
57 Adam R. and Davis, Kenneth J. and Herndon, Scott C. and Jacob, Daniel J. and Karion, Anna and Kort, Eric A. and Lamb,
58 Brian K. and Lauva, 2018; Ganesan et al., 2019). Moreover, the reports are based on indirect statistics, such as O&G inventories,
59 rather than direct measurements (Deng et al., 2022). This leads to a broad consensus that prominent discrepancies exist between
60 the reports. For example, field campaigns nearly double official claims of methane emissions in the United States by correcting
61 leak detection (Alvarez, Ramón A. and Zavala-Araiza, Daniel and Lyon, David R. and Allen, David T. and Barkley, Zachary
62 R. and Brandt, Adam R. and Davis, Kenneth J. and Herndon, Scott C. and Jacob, Daniel J. and Karion, Anna and Kort, Eric
63 A. and Lamb, Brian K. and Lauva, 2018).

64 To this end, widespread super-emitters present a unique opportunity worldwide (Duren et al., 2019; Lauvaux et al., 2022;
65 Pandey et al., 2019; Zavala-Araiza et al., 2015, 2017). Super-emitters can generally be defined to be emission sources that
66 comprise highly concentrated methane plumes and dominate localized methane budgets ($\sim 5 \times 5 \text{ km}^2$). In contrast to region-
67 scale hotspots (or area sources), they can be attributed to individual facilities (e.g., factories, chimneys, and pipelines), typically
68 with side lengths varying from several meters to tens of meters depending on monitoring instruments. Super-emitters are
69 typically responsible for the underestimates of methane emissions (Alvarez et al., 2018; Duren et al., 2019; Itziar et al., 2021;
70 Lauvaux et al., 2022; Thompson et al., 2016). Moreover, there is increasing evidence that methane emissions follow a heavy-
71 tailed distribution (Duren et al., 2019; Frankenberg et al., 2016; Lauvaux et al., 2022), for which relatively small number of
72 sources (so-called super-emitters) can account for a disproportionately large share of total emissions. In contrast to area sources
73 (e.g., cities), super-emitters are typically coal mines, wells, gathering stations, storage tanks, pipelines, and flares, with even
74 less than dozens of metres in diameter but high-concentrated methane plumes (Allen et al., 2013; Miller et al., 2019;

75 Subramanian et al., 2015; Varon et al., 2019). We thus anticipate that significant emission mitigation could be achieved by
76 deploying well-designed systems to identify methane super-emitters. For instance, in support of the Paris agreement, the 17th
77 World Meteorological Congress (2015) requested an Integrated Global Greenhouse Gas Information System (IG3IS) that
78 aimed to develop a measurement framework for methane emission reductions (Phil DeCola and WMO Secretariat, 2017).
79 To date, a large body of field measurements (e.g., in situ and aircraft surveys) between 2012 and 2020 has been designed for
80 methane super-emitters. Despite this, they are spatially confined (e.g., regionally) and temporally infrequent (e.g., a few weeks),
81 incapable of exploring global methane super-emitters (Alvarez, Ramón A. and Zavala-Araiza, Daniel and Lyon, David R. and
82 Allen, David T. and Barkley, Zachary R. and Brandt, Adam R. and Davis, Kenneth J. and Herndon, Scott C. and Jacob, Daniel
83 J. and Karion, Anna and Kort, Eric A. and Lamb, Brian K. and Lauva, 2018; Conley et al., 2016; Duren et al., 2019; Marchese
84 et al., 2015; Nisbet et al., 2020; Smith et al., 2017; Thompson et al., 2016; Thorpe et al., 2016). Today, substantial advances
85 have been made towards detecting and quantifying methane super-emitters from space (Cusworth et al., 2019; Hu et al., 2018;
86 Irakulis-Loitxate et al., 2022; Jacob et al., 2016; Pandey et al., 2019; Thompson et al., 2016) (Table 1). Such advances, however,
87 have rarely been expanded to measure the global methane pledge because large-scale swath and high-resolution sampling have
88 not been coordinated. First, global methane monitoring has become possible. A flagship satellite mission is the TROPOspheric
89 Monitoring Instrument (TROPOMI) onboard the Copernicus Sentinel-5 Precursor satellite (Lauvaux et al., 2022; Veeffkind et
90 al., 2012). It can offer daily global insights for methane column concentrations, with a large swath width of ~ 2600 km, a
91 moderate resolution of 7.0×5.5 km² (since August 2019), and high signal-to-noise ratios. However, its relatively coarse spatial
92 sampling still limits its application to detect methane super-emitters (Lauvaux et al., 2022). Second, next-generation satellite
93 missions, pioneered by the GHGSat constellation (three satellites at the moment), emerge for mapping methane super-emitters
94 (Cusworth et al., 2019), with a narrow swath (e.g., ~ 12 km) but a ground-breaking high-resolution spatial sampling (e.g., 25
95 ~ 50 m) (Jervis et al., 2021; Varon et al., 2020). Complementary to the GHGSat constellation, satellite-based hyperspectral
96 imager spectrometers, such as PRISMA, GF-5, ZY1, Sentinel-2, and Worldview-3, have shown great potentials (Guanter et
97 al., 2021; Itziar et al., 2021; Sánchez-García et al., 2021; Varon et al., 2021). They can resolve methane enhancements and
98 attribute them to specific infrastructures via similar narrow swath and high-resolution sampling (e.g., 30 m). Note that regions
99 those satellites usually gazed at are originally well-known home to methane super-emitters. Narrow swath coverage thus
100 remains a crucial limitation for global surveys of methane super-emitters. Collectively, existing studies still struggle to
101 surveillance global methane super-emitters due to the fact that individual satellite missions, either TROPOMI or PRISMA,
102 cannot coordinate large-scale swath and high-resolution sampling.

103 To address this issue, we present a two-tiered, space-based framework that coordinates TROPOMI and PRISMA for both
104 planet-scale and plant-level methane retrievals. The key is that ready-made satellite missions alone have the potential to initiate
105 immediate monitoring of the global methane pledge. Using this framework, we patrol the world, with an experimental focus
106 on China, the United States, Iraq, Kuwait, and Algeria, and reveal both region-scale hotspots and plant-level super-emitters.
107 We can even gaze at a single source to map multiple plumes and inspect possible methane leakages. These results can challenge
108 national reports that possibly miss unexpected super-emitters or mislead emission magnitude. On the eve of the Paris target,

109 at least while a global methane monitoring network is not in place, this multi-tiered satellite constellation presented in this
110 study has important implications for measuring global methane pledges.

111 **2. Materials and Methods**

112 **2.1 Multi-tiered satellite constellation**

113 The multi-tiered satellite constellation is designed to reconcile global-scale and high-resolution methane monitoring. First,
114 TROPOMI offers a unique potential for global methane monitoring, depending on its large-scale (i.e., 2600 km) swath, daily
115 revisit time, regional footprint (i.e., $5.5 \times 7 \text{ km}^2$ since August 2019), and sounding precision and accuracy (i.e., $< 1 \%$)
116 (Veefkind et al., 2012). Approximately, TROPOMI observes a full swath per second, resulting in ~ 216 spectra per second.
117 This instrument comprises two spectrometer modules, the first involving near-infrared (NIR) spectral channels, and the second
118 dedicated to the shortwave-infrared (SWIR) spectral channel. The NIR and SWIR channels are equipped with spectral
119 resolutions of 0.38 and 0.25 nm and spectral sampling ratios of 2.8 and 2.5, respectively. Since the NIR and SWIR detectors
120 are incorporated in different instrument modules, the NIR spectra will be co-registered with the SWIR spectra before
121 performing methane retrievals. The methane total column-averaged dry-air mole fraction (XCH_4) is retrieved from near-
122 infrared (NIR) (757 ~ 774 nm) and shortwave-infrared (SWIR) (2305 ~ 2385 nm) spectral measurements for sunlight
123 backscattered by Earth's surface and atmosphere (Hu et al., 2018). In this study, only high-quality measurements, retrieved
124 under cloud-free and low aerosol load conditions, are used. These measurements are filtered, in addition, for solar zenith angle
125 ($< 70^\circ$), low viewing zenith angle ($< 60^\circ$), and smooth topography (the surface elevation of < 80 m within 5 km radius) as
126 described in Hu et al. (28) (Hu et al., 2018).

127 Hyperspectral satellite missions serve as the second tier, responsible for mapping localized methane super-emitters depending
128 on their unprecedented resolution (i.e., 3m ~ 50m). Therein PRISMA, as an open-access representative, is specifically suitable
129 for this work. It can image the solar radiation reflected by the Earth's surface and atmosphere via hundreds of spectral channels
130 between the visible and SWIR spectrum ($\sim 400 \sim 2500$ nm). Measurements in the SWIR spectrum from 2000 to 2500 nm
131 sample absorption features from water vapor, carbon dioxide, and methane. Therein the 2100 nm and 2450 nm windows are
132 especially sensitive to methane. Furthermore, the signal-to-noise ratio is reported to be about 100 in the SWIR for a relatively
133 dark vegetation pixel and increases up to above 200 for bright soil surfaces in oil and gas extraction sites. More importantly,
134 it covers areas of $30 \times 30 \text{ km}^2$ with a 30 m spatial sampling.

135 We collect dozens of daily measurements from the multi-tiered satellite constellation. These measurements experimentally
136 map regional methane hotspots and localize methane super-emitters across the United States, China, the Middle East (Iraq and
137 Kuwait), and North Africa (Algeria). The acquisitions are mostly taken between April 2020 and January 2022.

138 2.2 Multi-tiered methane retrievals

139 In the first tier of our framework, we employ the operational methane products via TROPOMI onboard the Sentinel 5 satellite.
140 The target product is the column-averaged dry-air volume mixing ratio of methane (XCH_4), which will be retrieved
141 simultaneously with scattering properties of the atmosphere. The operational retrieval algorithm is based on RemoTeC (Butz
142 et al., 2009; Hasekamp and Butz, 2008), which is originally developed for CO_2 and methane retrievals from GOSAT
143 observations (Butz et al., 2011). It attempts to fit spectra observed by the TROPOMI-based NIR and SWIR channels. Its
144 sensitivities to atmospheric scattering properties, atmospheric input data, and instrument calibration errors have been
145 extensively evaluated (Sha et al., 2021; Verhoelst et al., 2021). As a result, the operational products are proved to be critically
146 stable, with a convergence rate of 99% and high significance as compared with both satellite-based (e.g., GOSAT) and ground-
147 based (e.g., TCCON) measurements. The required accuracy and precision of $< 1\%$ for the XCH_4 product are met for clear-
148 sky measurements over land surfaces and after appropriate filtering of difficult scenes. Moreover, the forward model error is
149 less than 1% for about 95% of the valid retrievals. Model errors in the input profile of water do not influence the retrieval
150 outcome noticeably. The methane product is expected to meet the requirements if errors in input profiles of pressure and
151 temperature remain below 0.3% and 2 K, respectively. Of all instrument calibration errors, the retrieval results are the most
152 sensitive to an error in the instrument spectral response function of the shortwave infrared channel.

153 In the second tier of our framework, we apply the matched-filter algorithm to calculate per-pixel methane enhancements with
154 respect to background levels based on the SWIR sample spectrum (i.e., the 2100 - 2450 nm window) onboard the PRISMA
155 (Foote et al., 2020; Guanter et al., 2021; Itziar et al., 2021). In theory, the retrieval method can depend on physically-based or
156 data-driven algorithms. The former aims to explicitly resolve the radiative transfer between the surface, the atmosphere, and
157 the hyperspectral spectrometers. A key representative is the family of differential optical absorption spectroscopy (DOAS)
158 methods (Cusworth et al., 2019, 2020, 2021b, 2021a). The latter seeks a methane absorption spectrum across a hyperspectral
159 image using statistical methods. It is commonly based on the matched-filter and the singular vector decomposition concepts.
160 These methods are both widely applied and evaluated, especially onboard satellite (e.g., PRISMA, GF-5, and ZY-1) and
161 airborne (e.g., AVIRIS and AVIRIS-NG) platforms (Cusworth et al., 2020; Foote et al., 2020; Guanter et al., 2021; Itziar et
162 al., 2021; Thompson et al., 2016; Thorpe et al., 2016). In this study, the data-driven retrieval based on the matched-filter
163 concept is used. The main reason is that it could implicitly account for potential radiometric and spectral errors in satellite-
164 based imaging spectroscopy. For instance, vertical striping is prevalent in hyperspectral measurements due to detector
165 inhomogeneity, thus substantially degrading methane retrievals. The matched-filter algorithm focuses on the individual
166 columns rather than the whole scene to resolve methane enhancements. This means that the methane enhancement per column
167 is calculated separately (i.e., methane enhancements were calculated on a per-column basis). More explanations can be found
168 in Guanter et al. (2021). Besides, the physically-based method has to consider background concentrations that are difficult to
169 determine around the super-emitters. In contrast, the data-driven method is independent of background levels and can directly

170 seek methane enhancements. Finally, the data-driven method generally has a substantially superior computational efficiency
171 compared to the physically-based method.

172 The matched-filter retrieval used here is similar to the one used by Thompson et al. (2016) for the Hyperion imaging
173 spectrometer onboard the EO-1 satellite. The calculation processes of methane enhancements ($\Delta\mathbf{XCH}_4$, **ppb**) are as follows.

174
$$\Delta\mathbf{XCH}_4(\vec{\mathbf{x}}) = \frac{(\vec{\mathbf{x}} - \vec{\boldsymbol{\mu}})^T \boldsymbol{\Sigma}^{-1} \vec{\mathbf{t}}}{\vec{\mathbf{t}}^T \boldsymbol{\Sigma}^{-1} \vec{\mathbf{t}}} \text{ (Eq. 1).}$$

175 The $\vec{\mathbf{x}}$ denotes the spectrum under analysis. The $\vec{\boldsymbol{\mu}}$ and $\boldsymbol{\Sigma}$ represent the mean background radiance and corresponding
176 covariance, respectively, calculated with their common formulas after subtracting the current signal estimates from the data.
177 Specifically, the $\vec{\boldsymbol{\mu}}$ is calculated from the data with the removal of the most recent enhancement estimates, while the $\boldsymbol{\Sigma}$ is then
178 calculated with updated $\vec{\boldsymbol{\mu}}$ and the most recent enhancement estimates. More technical details are reported in previous studies
179 (Foote et al., 2020). Note that, owing to the non-uniform response of individual detectors in PRISMA, they are calculated
180 based on per-column spectrums in order to consider different responses of across-track sensors to radiance. The $\vec{\mathbf{t}}$ is the target
181 spectrum that reflects the background radiance enhanced by the methane plume. It is generated by the elementwise
182 multiplication of $\vec{\boldsymbol{\mu}}$ and $\vec{\mathbf{k}}$. This implicit parameter $\vec{\mathbf{k}}$ represents a unit methane absorption spectrum derived from a look-up
183 table simulated by the MODTRAN radiative transfer model. Similarly, the spectral convolution is also performed on a per-
184 column basis.

185 In principle, it would be more difficult to detect methane enhancements in pixels over low-albedo surfaces. Although methane
186 absorption is independent of albedo, the resulting signal in absolute radiance is weakened with surface albedo decreasing. A
187 major measure to compensate for the albedo effect is to scale the target spectrum $\vec{\mathbf{t}}$ by the pixel-specific albedo factor due to
188 the fact that the Beer–Lambert absorption law depends on the initial radiance in the absence of the absorber. Here the pixel-
189 specific scalar \mathbf{f} is calculated based on the spectral average $\vec{\boldsymbol{\mu}}$ and the analysis spectrum $\vec{\mathbf{x}}$ as follows:

190
$$\mathbf{f} = \frac{\vec{\mathbf{x}}^T \vec{\boldsymbol{\mu}}}{\vec{\boldsymbol{\mu}}^T \vec{\boldsymbol{\mu}}}. \text{ (Eq. 2)}$$

191 This solution makes $\Delta\mathbf{XCH}_4$ normalized by the albedo term, similar to the per-pixel normalization in previous hyperspectral
192 analysis (Kraut et al., 2005). The premise to launch the matched-filter algorithm is the accurate knowledge of the response of
193 the instrument spectra to the methane absorption nature. To this end, the objective is to gain the best fit between the simulated
194 and reference spectra. An initial step is thus conducted to update the spectral calibration for the channels within the 2100 -
195 2400 nm window, in which the channel wavelength centre and width are updated for each across-track position in each scene.
196 Other details are illustrated in previous attempts (Foote et al., 2020; Guanter et al., 2021; Irakulis-Loitxate et al., 2022).

197 **2.3 Multi-tiered attribution of methane hotspots and plumes**

198 In the first tier of our framework, we apply visual inspection to identify methane hotspots using the TROPOMI-based methane
199 retrievals. The transformation from visual inspection to automatic recognition would significantly advance long-term, global
200 methane monitoring. However, no satisfactory set of criteria was found that could be suitable for this study. This was mainly

201 because, in localized regions, methane budgets respond to the changes in not only super-emitters but also complex external
202 factors (e.g., meteorology, topography, and background concentrations). Similar compromises are also adopted in previous
203 studies. Therefore, automatic recognition enabled by artificial intelligence would play an essential role in the versatile
204 spaceborne architecture for long-term, global methane monitoring (Ouerghi et al., 2021; Paoletti et al., 2018; Yang et al., 2018;
205 Yu et al., 2017; Zhang et al., 2018).

206 Regarding the identified methane hotspots, we utilize a Boolean mask to select plume-influenced pixels downwind of the
207 source. The background distribution (mean \pm standard deviation) is defined by an upwind sample of the measured columns, in
208 which the hourly wind field data come from the ERA5 reanalysis dataset produced by the European Centre for Medium-Range
209 Weather Forecasts (ECMWF) (Hoffmann et al., 2019). We then sample the surrounding (5×5) pixels centred on each pixel
210 and compare the corresponding distributions to the background distribution based on a Student's t-test. Pixels with a
211 distribution substantially higher than the background at a confidence level of 95% are assigned to the plume. More details in
212 the Boolean plume mask can be found in previous studies (Pandey et al., 2019; Varon et al., 2018).

213 Regarding the identified regional hotspots, we also apply visual inspection to search for plumes within their surrounding 30
214 km scales (i.e., corresponding to the swath width of PRISMA) in the second tier of our framework (Itziar et al., 2021; Lauvaux
215 et al., 2022; Martin et al., 2018; Varon et al., 2020). To date, it is still challenging to distinguish methane plumes in
216 hyperspectral images using full physically-based algorithms. The main cause is potential methane retrieval artifacts from
217 hyperspectral satellites that are spatially correlated to surface features. Specifically, we manually search for methane
218 enhancement pixels with gas-plume-like shapes, i.e., high methane enhancements progressively decrease downwind. The
219 resulting pixels are subsequently compared to the spectral radiance data at the 2300 nm absorption feature sensitive to low
220 surface albedos. In this way, the fake positives due to specific surface features are prevented. On this basis, the candidate pixels
221 are overlaid over simultaneous (i.e., hourly) wind fields and high-resolution imageries in individual scenes. They would be
222 considered to be true plumes if they roughly align with simultaneous wind direction and origin from explicit infrastructures.
223 Here the high-resolution satellite imageries are taken from the Google Map. The hourly wind field data also come from the
224 ERA5 reanalysis dataset. Finally, we manually draw polygons to mask such resulting plumes out. As preparation for plume
225 emission quantification, we remove the background using the threshold of the median values of the scenes.

226 These satellite imageries allow us to categorize methane plumes within narrow spatial scales between 50 to 500 m², such as
227 O&G extraction platforms, storage tanks, and compressor stations. They even enable the attribution of plumes to specific
228 emission ports in individual sources due to their very high resolution. Furthermore, we could name them based on points of
229 interest in the Google Map. On this basis, such sources could be visually retrospected via long-term, high-resolution (i.e., 10
230 m) satellite images from the Sentinel-2 mission (Ehret et al., 2021; Varon et al., 2021). Their key details, like ages and statuses
231 (e.g., active or inactive), are thus collected reliably. Note that, regarding such information, national reports are typically
232 credible but inaccessible, particularly in global missions. In addition, it should be highlighted that, on top of considerably high
233 budgets, like megacities, there must be super-emitters undetectable in our way. Other causes are discussed in uncertainty
234 analysis in Supplement Information.

235 2.4 Multi-tiered quantification of methane emissions

236 In our framework, we calculate the total excess mass of methane in kilograms in the detected hotspots (in the first tier) and
237 plumes (in the second tier) using the so-called integrated mass enhancement (IME) model (Frankenberg et al., 2016; Varon et
238 al., 2018). To make conservative estimates, we define the background levels as the 10% of the average methane concentrations
239 in the TROPOMI-based and PRISMA-based scenes (Figs. 1b ~ 1g) (Frankenberg et al., 2016; Varon et al., 2018). On this
240 basis, we eliminate the interferences from the background concentrations and calculate IMEs as the methane masses of the
241 masked hotspots and plumes.

242 Overall, this method links the emission rate (Q) with the measured IME via the residence time of methane (IME/Q). This
243 residence time relies on an effective wind speed (U_{eff}) and a characteristic plume size (L) as follows:

$$244 \quad Q = \frac{U_{\text{eff}} \cdot \text{IME}}{L}. \quad (\text{Eq. 3})$$

245 Specifically, the IME and L can be inferred from the observations of the hotspots or plumes. During this process, we carefully
246 apply a Boolean plume mask that separates the pixels (i) with notable signals ($\Delta\Omega_i$) from background pixels and thus defines
247 the total areas ($\sum_{i=1}^N A_i$) of the hotspots or plumes. The L is defined as the square root of the total plume areas. Hence, the IME
248 is calculated as follows:

$$249 \quad \text{IME} = \sum_{i=1}^N \Delta\Omega_i A_i. \quad (\text{Eq. 4})$$

250 In the first tier of our framework, the effective wind speed (U_{eff}) is defined as the 10-m wind speed U_{10} obtained from the
251 ERA5 reanalysis dataset. According to the detected hotspot, the value at the nearest hour and location are used.

252 In the second tier of our framework, we apply an ensemble of large eddy simulations (LES) to establish an empirical, linear
253 relationship between U_{eff} and the measured 10-m wind speed U_{10} as follows (Fig. S8)

$$254 \quad U_{\text{eff}} = 0.8602 \ln(U_{10}) + 1.1513. \quad (\text{Eq. 5})$$

255 The configurations of these simulations, such as spatial resolution and precision, are comparable to our PRISMA data. Other
256 details in this methodology were described in Varon et al. (2018) (Varon et al., 2018).

257 We estimate the uncertainties of Q by propagating the random errors in U_{10} and IME . This processes are conducted in previous
258 studies (Cusworth et al., 2019, 2021b; Itziar et al., 2021). As shown in previous findings, the major error source come from
259 the U_{10} term. Its random distributions typically correspond to the 50% random error. On this basis, this error is integrated
260 quadratically with the standard error of the IME , the result of which can be treated as the final random error of Q . The intrinsic
261 errors of the IME model are quantified in the following uncertain analysis.

262 2.5 Uncertainty Analysis

263 The objective of this work is to promote a multi-tiered satellite constellation that can monitoring global methane pledges. To
264 better understand the performance of our framework, we conduct comprehensive uncertain analysis. Note that the protocol of
265 the uncertain analysis on our framework origins from previous studies (Itziar et al., 2021; Varon et al., 2020). Specifically, we
266 require to account for the uncertainties in the TROPOMI-based and PRISMA-based methane retrievals and subsequent

267 emission estimates. Therein the operational TROPOMI-based methane retrieval products have been evaluated strictly and
268 proved to be reliable globally (except in low- and high-albedo and snow-covered areas) (Lorente et al., 2021; Sha et al., 2021).
269 In this work, we thus focus on three main sources of uncertainties, specifically including (1) uncertainties in the PRISMA-
270 based methane retrievals; (2) uncertainties in the TROPOMI-based methane emission estimates; and (3) uncertainties in
271 PRISMA-based methane emission estimates. During the analysis for the latter two uncertain sources, we would further
272 investigate the potential wind impacts on the methane emission estimates. Note that it remains challenging to directly quantify
273 the uncertainties in the wind fields across our cases due to the lack of measurements. We would thus assess the variations in
274 the methane emission estimates driven by distinct wind data. From such analysis, we could confirm the reliable performance
275 of our framework. Details can be found in Supplementary Information.

276 The detection limit of this framework depends mainly on the TROPOMI-based and PRISMA-based methane retrievals, which
277 have been well discussed in previous studies (Guanter et al., 2021; Hu et al., 2018). As the robust relationship between the
278 “minimum source” and the related methane enhancement interpreted by Jacob et al. (2016) and Guanter et al. (2021), the
279 detection threshold for the TROPOMI instrument is 4000 kg/h with a wind speed of 5 km/h. Following the same relationship
280 in the PRISMA instrument, we estimate that a retrieval precision of 114 ppb (6.1% with the assumed background concentration
281 of 1850 ppb), such as in the case of the Hassi Messaoud site (Fig. S10e1), would lead to a detection limit of 800 kg/h for the
282 same wind speed (analogous to the reported range of 500 ~ 900 kg/h) (Guanter et al., 2021; Irakulis-Loitxate et al., 2022).
283 Similar instruments and detection limits are generally comparable to emissions from anthropogenic sectors, like O&G and
284 coal mines in this study or landfills, agriculture, and waste management in previous studies (Lauvaux et al., 2022; Maasackers
285 et al., 2023; Sadavarte et al., 2021). However, no conclusive evidence shows by far that short-term (e.g., daily) satellite-based
286 measurements with such detection limits can capture methane hotspots driven by natural sources (e.g., wetlands). In contrast,
287 long-term (e.g., year-round) satellite-based measurements with much higher detection limits have shown the potential (Pandey
288 et al., 2021).

289 **3 Results and discussions**

290 **3.1 Multi-tiered imaging of global methane hotspots and super-emitters**

291 Figure 1 presents representative sets of methane hotspots and associated super-emitters across the United States, China, the
292 Middle East (Iraq and Kuwait), and North Africa (Algeria) via our multi-tiered satellite constellation. Each group first clarifies
293 a methane-abundant region and further focuses on explicit super-emitters. Among them, five methane-abundant regions are
294 captured in Wattenberg (the United States), Yangquan (China), Rumaila (Iraq), Burgan (Kuwait), and Hassi Messaoud (Algeria)
295 (Fig. 1a and Table S1). These account for 4805 ~ 46138 kg/h methane emissions based on our daily first-tiered (i.e.,
296 TROPOMI-based) monitoring. From the perspective of a state-of-the-art global methane emission inventory (i.e.,
297 EDGARv6.0), such high values rank among the top 1% regarding emission intensities per unit area (km²) (Fig. S1) (Crippa et

298 al., 2020). The Rumaila field, for example, is known as the largest oil field in Iraq (in terms of both reserves and yields). In
299 this work, it is found with a significant methane emission intensity exceeding 45000 kg/h (Fig. 1b). In addition to such well-
300 known oil fields (Figs. 1c ~ 1f), methane hotspots emerge in developing coal mines, like Yangquan, with comparable emission
301 levels (> 30000 kg/h) (Fig. 1g).

302 We attribute these methane enhancements to specific methane plumes via the second-tiered (i.e., PRISMA-based) monitoring
303 (Figs. 1b1 ~ 1g2). There are substantial variations in the methane plumes' amounts, types, and magnitude, even in a single
304 methane-abundant region. For instance, in the Burgan field, the second-tiered monitoring detects up to eight methane plumes
305 in a handful of grids in the first-tiered monitoring (Figs. 1c1 ~ 1c4 and 1d1 ~ 1d4). Such intensive distributions are also found
306 in previous region-oriented surveys in the Permian basin and California (Duren et al., 2019; Itziar et al., 2021). Together with
307 high-definition images (Fig. S2), we find that such plumes origin from various sources, such as flares, factories, and wells. A
308 breakthrough is the capture of two distinctive plumes in an individual methane source with extremely high emissions (> 10000
309 kg/h), unprecedented in previous satellite-based exploration and only observable in aircraft surveys (Fig. 1b1). Such precise
310 distinctions benefit from the high resolution of the second-tiered monitoring, despite being limited by the relatively higher
311 detection threshold (~ 300 kg/h) (Guanter et al., 2021). Besides, factories and wells can also emit such evident plumes (Fig.
312 1c1 and Figs. 1e1 and 1e2). By comparison, other plumes are typically more diffuse but with comparable emission magnitude
313 ($\sim 1000 \sim 7000$ kg/h).

314 Note that the above results represent only snapshots at the overpass moments of the satellites (i.e., TROPOMI and PRISMA)
315 (Figure 1). Specifically, for a given set (including both a methane-abundant region and associated super-emitters), the overpass
316 timing of TROPOMI can be nearly concordant with that of PRISMA. The temporal gaps could be frequently controlled within
317 ten days (e.g., Figs. 1b and 1d), even two days (Figs. 1e, 1f, and 1g). For instance, within only two days (August 18th and 19th,
318 2021, November 15th and 17th, 2021), our multi-tiered satellite constellation goes through the Hassi Messaoud field and the
319 Yangquan coal mine and provides in-depth views of methane budgets, including methane-abundant regions and their drivers
320 (Figs. 1e and 1g). Even, in just one day (July 7th, 2021), our multi-tiered satellite constellation not only uncover methane
321 enhancements in the Wattenberg field (Fig. 1f) but also track them back to explicit methane super-emitters (Figs. 1f1 and 1f2).
322 As expected, if we extend the monitoring window of our framework to years, more methane super-emitters are subsequently
323 captured (Fig. S3). Moreover, our framework via multi-tiered satellite constellation paves an in-time way for routine
324 monitoring of global methane hotspots and associated super-emitters.

325 **3.2 Multi-tiered verification of global methane super-emitters**

326 Four unexpected cases occur in Burgan (Iraq), Hassi Messaoud (Algeria), and Yangquan (China), potentially explainable if
327 we take mutual verification of the first- and second-tiered monitoring into consideration. First, an anomalous methane plume
328 is detected in the Burgan field (Fig. 1c4) of high emission magnitude (> 1500 kg/h), notably exceeding typical O&G facilities,
329 from an elusive source (i.e., no clear source could be attributed) (Fig. S2). The long-term measurements of our multi-tiered

330 satellite constellation intermittently, rather than accidentally, observe this abnormal plume (Figs. S4). Furthermore, uncertain
331 analysis (see Materials and Methods) helps to confirm this real plume. In particular, the methane plumes are clearly
332 uncorrelated with the surface brightness from space (Fig. S4). Consequently, the most likely hypothesis for this super-emitter
333 is methane leakage from gigantic O&G pipelines as shown in the Google Map (Fig. S2).

334 Second, we observe suspect trails of methane plumes above the storage tanks in the Burgan field (Fig. 1d4). Conceivably, the
335 technical noise driven by albedo effects bore the brunt, although it is believed to be corrected reliably (See Materials and
336 Methods). To this end, we apply a multi-spectral retrieval algorithm to eliminate this effect to a large extent. The detailed
337 illustrations are shown in Supplementary Information (Fig. S5). Consequently, we provide evidence that un-negligible methane
338 emissions (> 3500 kg/h) may very well be the unique explanation, likely related to fugitive methane leaks from the storage
339 tanks. This is only seen in previous aircraft-based surveys (Frankenberg et al., 2016). Therefore, our multi-tiered outcomes
340 indicate even more widespread methane leaks than expected. Note that the multi-spectral retrieval algorithm cannot completely
341 remove the albedo effects on our framework. As such, our framework could lead to efficient on-site re-inspection on worldwide
342 and innumerable O&G fields.

343 Third, our framework detect a new methane super-emitter in the Hassi Messaoud field on December 7, 2021 (Fig. 1e4). By
344 revisiting historical satellite images in the second-tiered monitoring (Fig. S6), we could confirm that this super-emitter arose
345 between October 18th and November 12, 2021. These results indicate that monitoring of global methane super-emitters can
346 attain monthly resolution via current satellite constellation alone. Conceivably, more satellite observations would further close
347 the time window. Fourth, a distinct methane plume appears in a coal mine in a mountainous area (Yangquan, China), exceeding
348 all of the detected O&G super-emitters regarding the emission rate (> 7000 kg/h) (Fig. 1g1).

349 Figure 2 illustrates that, in our multi-tiered satellite constellation, the extent to which the explicit plumes in the second tier
350 explain the regional budget detected by the first tier. The overpass moments are explicitly shown Fig. 1, most of which are
351 inconsistent between for the first- and second-tier monitoring. Overall, the plumes in the former are mostly responsible for
352 large shares ($> 8.2\%$) of regional budgets in the latter. In the Rumaila, Burgan, and Wattenberg fields, the detected methane
353 plumes play a more critical role, with contributions up to $53.8 \sim 65.9\%$. Note that such contribution estimates might
354 occasionally exceed 100% mainly owing to the inconsistent overpass moments between the first- and second-tier monitoring.

355 By comparison, the relatively low but still significant contributions in the Hassi Messaoud field (8.2%) and Yangquan coal
356 mine (35.7%) are partly due to the technical limitation of our framework in detecting methane plumes on top of high
357 background levels. Collectively, the heavy-tail law of methane plume distributions, early reported for regional O&G fields
358 (like the Permian basin and California) (Duren et al., 2019; Itziar et al., 2021), is possibly applicable worldwide. To further
359 explore such a hypothesis, we extend the temporal sample window of our multi-tiered framework. Using year-round snapshots
360 in the second tier of our framework, we inspect the identified super-emitters (Figs. 1b ~ 1g) repeatedly and find more methane
361 plumes as expected (Fig. S3). This reinforces the above hypothesis for the widespread occurrence of methane super-emitters.

362 Note that there are differences in the order of magnitude between the TROPOMI-based and PRISMA-based results. The main
363 cause is that the TROPOMI-based and PRISMA-based results represent the methane emissions from different special scales.

364 The former results represent region-scale methane budgets, while the latter ones resolve the emission magnitude from the
365 individual methane super-emitter therein (Fig. 1). Although the latter results can explain a large fraction of the former ones
366 (Fig. 2), the gaps remain mainly due to inconsistent overpass moments between the two-tiered results or sources still missed
367 by the PRIMSA-based results. In other words, closing the temporal gaps between the two tiers or improving the detection
368 ability of the second tier would help to reconcile the first- and second-tiered results.

369 A regional survey in a California field is considered as the best reference, owing to its utilization of systematic airborne
370 measurements to detect and quantify methane super-emitters (Duren et al., 2019). The California survey aims to provide the
371 first view of methane super-emitters across the state. This survey is conducted with the Next Generation Airborne
372 Visible/Infrared Imaging Spectrometer (AVIRIS-NG), with 5 nm SWIR spectral sampling, 1.8 km view field, 3 m horizontal
373 resolution, and 3 km cruise altitude, and contains five campaigns over several months from 2016 to 2018. Moreover, this
374 instrument is unique due to its high signal-to-noise ratio and is capable of characterizing methane super-emitters with emissions
375 as small as $2 \sim 10$ kg/h for typical surface winds of 5 m/s. They survey reports 1181 methane plumes, more than 500 times
376 larger than previous aerial studies (Englander et al., 2018), with a median emission intensity of 170 kg/h. These results are
377 thus used to directly evaluate the outcomes in the second tier (Fig. 3). Even though some regions of interest in this study are
378 far less famous than the California field, their emission intensities are much higher. Specifically, these plumes detected by the
379 second-tiered monitoring have emission intensities (1142 ~ 11698 kg/h) that exceed the median value in the California field.

380 Satellite-based surveys are conducted repeatedly for the Permian basin (one of the top O&G basins worldwide) from 2019 to
381 2020 (Fig. 3). The Permian survey takes advantage of imaging spectroscopy technologies to provide the first spaceborne
382 region-scale and high-resolution survey of methane super-emitters in the Permian basin. This survey is acquired by 30
383 hyperspectral images from three satellite missions, including Gaofen-5, ZY1, and PRISMA, and focuses on an area of roughly
384 200×150 km² in the Delaware sub-basin of the Permian basin within several days (mostly on four different dates: 15 May
385 2019, 1 November 2019, 29 December 2019, and 8 February 2020). More technical details on these two surveys can be found
386 in previous studies (Duren et al., 2019; Itziar et al., 2021). Compared to the surveys in the California field, those in the Permian
387 basin achieves a much higher number of strong methane super-emitters, the median emission rates (1850 kg/h) much closer to
388 ours (2888 kg/h). Collectively, although such comparisons are not quantitative comparisons due to measurement divergencies
389 between these datasets (e.g., spatial resolution and detection limit), they offer further context for the emission magnitude of
390 the identified methane super-emitters and indicate the outstanding strength of our results that could be analogous to abundant
391 outcomes from field campaigns. More importantly, this highlights the urgent need for global monitoring of ‘nameless’ O&G
392 facilities that possibly emit methane as much as the California field and Permian basin.

393 **3.3 Multi-tiered challenges of national emission inventories**

394 These multi-tiered results challenge traditional methane emission inventories (Fig. 4). Here the conventional emission data is
395 obtained from a state-of-the-art bottom-up emission inventory (i.e., EDGARv6.0) for the year 2018. Consequently, for the

396 methane hotspots, this inventory is mostly consistent with the present results (-49.9 ~ 91.8%), with a fine average bias (63.2%).
397 The Hassi Messaoud field in Algeria is a unique exception, where the O&G sector is in rapid development, with a relatively
398 larger bias (489.2%). By comparison, this inventory significantly undervalues the methane super-emitters (up to orders of
399 magnitude). This indicates that traditional emission inventories might have acceptable performance for traditional methane-
400 abundant regions while incapable of tracking methane super-emitters.

401 First, outdated spatial proxies might explain the large divergence between our plant-based estimates and the EDGARv6.0 (Fig.
402 1b1 and Fig. S7). Moreover, the EDGARv6.0 is designed for the year 2018, missing the newly established O&G plants with
403 high methane emissions. Second, in principle, conventional inventories directly miss high emissions caused by abnormal
404 operations (e.g., equipment failures) (Fig. 1c4 and Fig. S8) such as the O&G blowout shown in on-site surveys (Pandey et al.,
405 2019). A compromise is downwind measurements, yet insufficiently reliable as shown in previous findings (Alvarez, Ramón
406 A. and Zavala-Araiza, Daniel and Lyon, David R. and Allen, David T. and Barkley, Zachary R. and Brandt, Adam R. and
407 Davis, Kenneth J. and Herndon, Scott C. and Jacob, Daniel J. and Karion, Anna and Kort, Eric A. and Lamb, Brian K. and
408 Lauva, 2018).

409 In addition, the relatively low bias in the Rumaila and Hassi Messaoud fields might be explained by other causes (Figs. 1b2
410 and 1e3) such as outdated emission factors. Empirically, a plant-level inventory, once optimized by direct measurements, can
411 raise total methane emissions by ~ 60%, although source categories vary substantially (Alvarez, Ramón A. and Zavala-Araiza,
412 Daniel and Lyon, David R. and Allen, David T. and Barkley, Zachary R. and Brandt, Adam R. and Davis, Kenneth J. and
413 Herndon, Scott C. and Jacob, Daniel J. and Karion, Anna and Kort, Eric A. and Lamb, Brian K. and Lauva, 2018). Besides,
414 temporal variability might also explain top-down and bottom-up differences in methane emission estimates. For instance, the
415 peak emission rate could exceed 40% higher than the average, which might occur in the middle afternoon due to specific
416 processes, like episodic venting from manual liquid unloading (Vaughn et al., 2018). This aligns with the sampling time of the
417 satellites, thus biasing bottom-up inventories. Collectively, it is necessary to carefully consider all factors affecting methane
418 emissions, including emission factor updating and spatiotemporal variations, in order to develop effective strategies for
419 mitigating methane emissions.

420 **3.4 Implications for global methane monitoring**

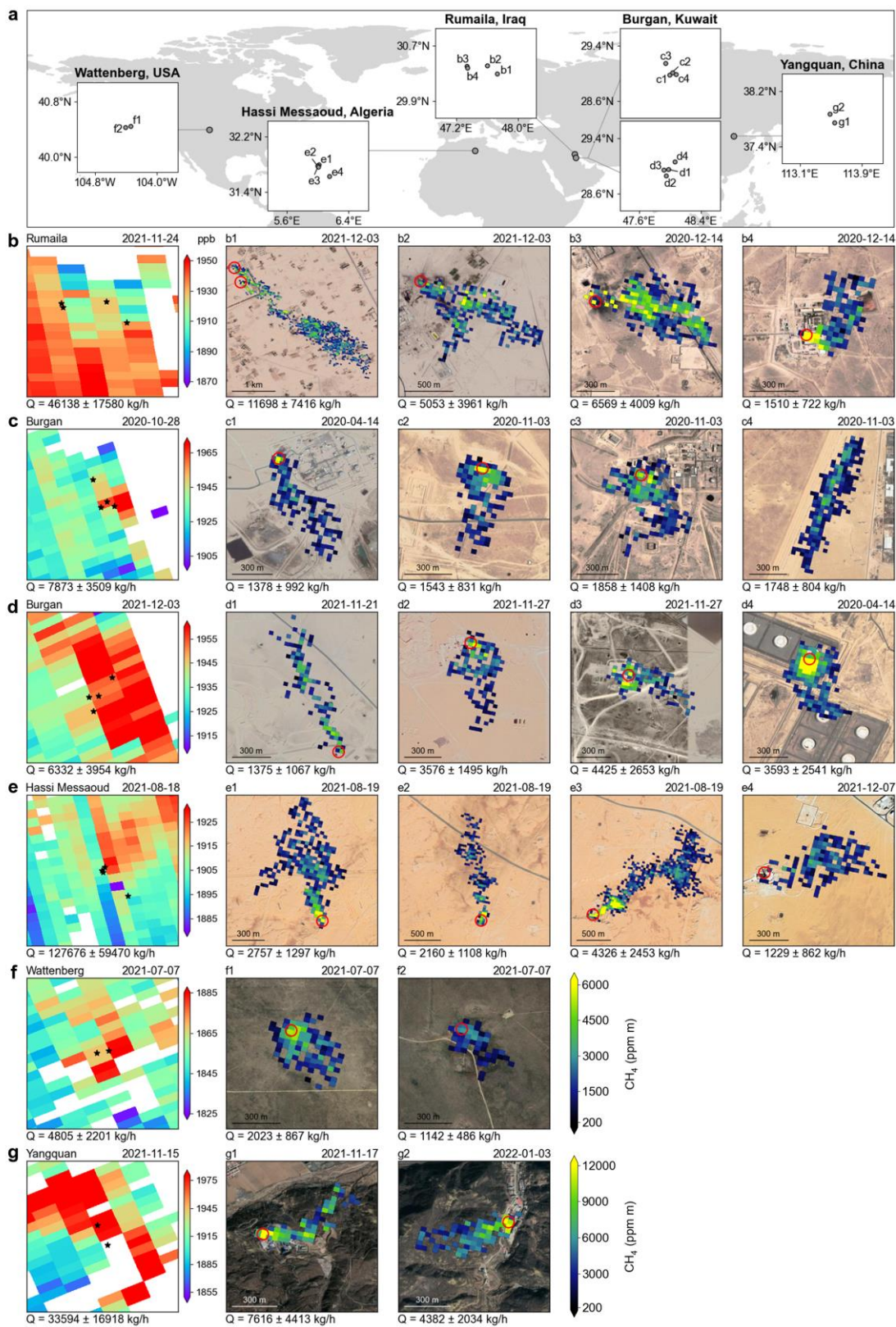
421 We present a multi-tiered, space-based framework that can harmonize planet-scale and plant-level methane retrievals (Fig. 5).
422 Using this framework, we patrol the world, with synergistic, proactive detections on the methane-abundant regions and
423 methane super-emitters across the United States, China, the Middle East (Iraq and Kuwait), and North Africa (Algeria). We
424 even lock new methane super-emitters, track potential methane leakages from storage tanks, and distinguish multiple methane
425 plumes in a single source. Such achievements are mostly unprecedented in satellite surveys and only observed in aircraft
426 campaigns. On this basis, our results challenge national reports that possibly miss unexpected super-emitters or mislead
427 emission magnitude, partly due to surges of oil and gas (O&G) facilities and widespread abnormal operations.

428 Our data prove that depending on ready-made satellite missions alone can initiate immediate, proactive monitoring of global
429 methane pledges, in contrast to existing surveys that have to focus on a priori methane-abundant regions. As such, as the
430 window for achieving the Paris target is rapidly closing, we will not need to sit back and wait for upcoming space missions,
431 like MethaneSAT and SBG in the United States, EnMAP in Germany, a new version of GF-5 in China, and, later, the European
432 Space Agency's CHIME from 2025 to 2030 (Cusworth et al., 2019). In addition, while scientific communities persistently
433 debates the drivers of the recent methane surge (Nisbet et al., 2014, 2019; Turner et al., 2019), the consequences of our
434 outcomes are clear, not only holding clues but also facilitating mitigation.

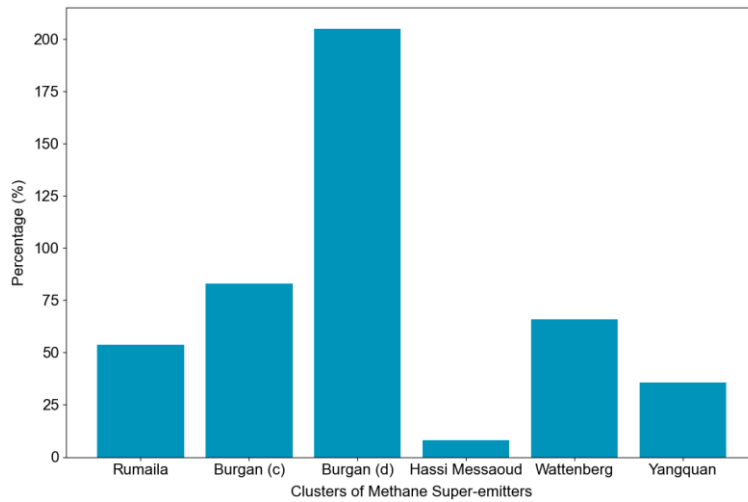
435 It should be noted that the multi-tiered framework is sustainable (Fig. 5). First, it can harmonize multiple satellites. The
436 potential representatives include upcoming official missions (e.g., the GF-5) (Itziar et al., 2021), current private constellations
437 (e.g., the GHGSat series) (Jervis et al., 2021; Varon et al., 2020), and explorable multispectral products (e.g., the Worldview-
438 3 and Sentinel-2) (Sánchez-García et al., 2021). Second, the framework is not confined to satellites and can be expanded by
439 integrating in situ (e.g., Global Atmosphere Watch Programme) (World Meteorological Organization, 2022), aircraft, and
440 unmanned aerial vehicles (UAVs) (Cusworth et al., 2020; Gålfalk et al., 2021; Tuzson et al., 2020). Note that such a multi-
441 tiered framework based on multifarious satellites, aircrafts, and UAVs keeps pursuing wider coverages and faster revisits. We
442 would thus derive the next objective in this manner, i.e., how to achieve effective, efficient, and economic monitoring of global
443 methane pledges, in which how to make better coverage-resolution balance between instruments is crucial. This will be the
444 topic of the next separate study. Third, nighttime methane monitoring is important because abnormal leakages or pulses might
445 also occur during nighttime (Plant et al., 2022; Poindexter et al., 2016). In these events, the LIDAR-equipped ones (involving
446 satellites, e.g., MERLIN) can allow to retrieve methane fluxes at all-latitudes, all-seasons, and all-weather (involving nighttime)
447 as they are not relying on sunlight. Third, better characterizing methane vertical profile would help to optimize our analysis,
448 like minimizing the uncertainties in tropospheric air mass factors and subsequent methane enhancements. Finally, on the basis
449 of our framework, rapid advances in artificial intelligence (AI) techniques are projected to completely replace manpower to
450 seek faint signals of methane enhancements in Earth's surface, and to significantly optimize data-driven algorithms of methane
451 emission estimates (Reichstein et al., 2019; Yuan et al., 2020). In principle, subsequent mitigation of such super-emitters via
452 routine maintenances, leak detections, or emergent repairs can provide effective, efficient, and economic solutions toward the
453 Paris target (Mayfield et al., 2017).

454 These outcomes have important ramifications for low- and middle-income countries. World powers, like the United States and
455 European Union, lead new national methane pledges. They are separately on the way to creating vast operational infrastructures
456 to monitor ambitious climate goals. Still, huge holes remain in coverage and authority, at least by the middle of this decade.
457 This situation is especially worse for low- and middle-income countries, where the tight budget dims the hopes for filling up
458 those holes by 2030, while methane emissions are likely to rise as countries develop. In this context, the present framework
459 can at once serve as the cost-effective piece of the global methane monitoring network and thus support fair climate
460 negotiations between countries.

461

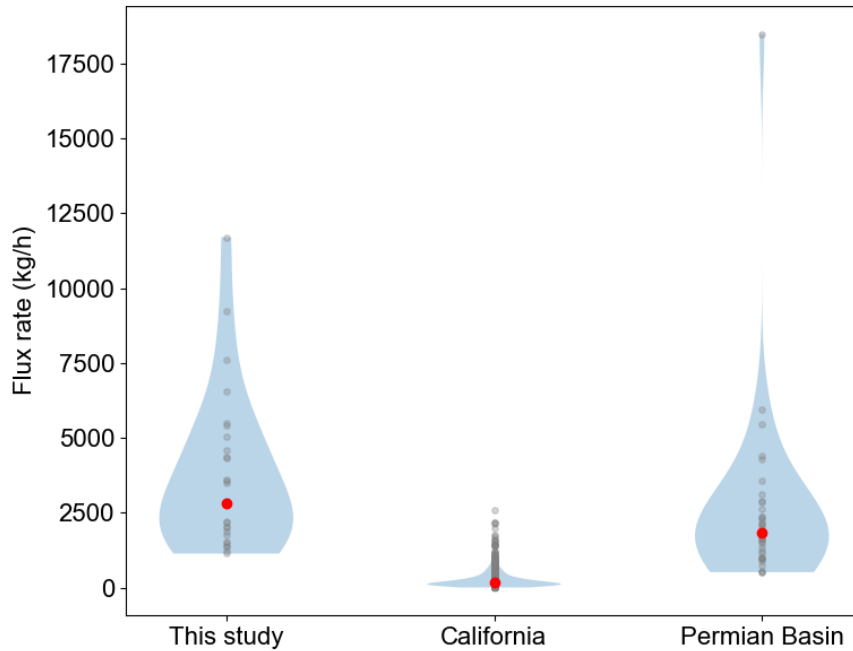


463 **Fig. 1. Methane hotspots and associated super-emitters across the United States, China, Iraq, Kuwait, and Algeria via**
464 **the multi-tiered daily satellite constellation.** (a) Methane-abundant regions and associated super-emitters are captured by
465 the TROPOMI and PRISMA, respectively. Their locations are marked by black rectangles and dots. Their names are obtained
466 from the Google Map, usually being the names of the nearest O&G fields and coal mines. (b ~ g) Each group clarifies a
467 methane-abundant region and explicit super-emitters (b1 ~ b4, c1 ~ c4, d1 ~ d4, e1 ~ e4, f1 ~ f2, and g1 ~ g2). For each super-
468 emitter (five-pointed stars), the overpass moments of the multi-tiered satellite constellation and the consequent emission
469 estimate are presented. Its base map is obtained from the Google Map. The second color bar for the PRISMA is suitable for
470 the super-emitters in China, while the first is for other countries. Plume sources in the PRISMA results are marked by red
471 circles.



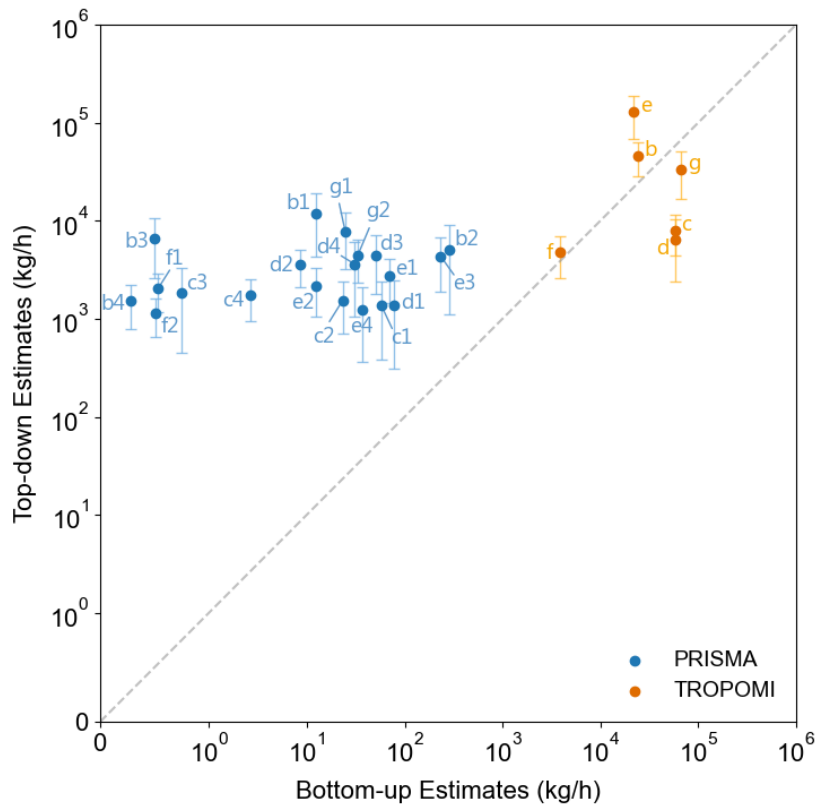
472

473 **Fig. 2. High contributions of methane super-emitters to corresponding regional methane budgets.**



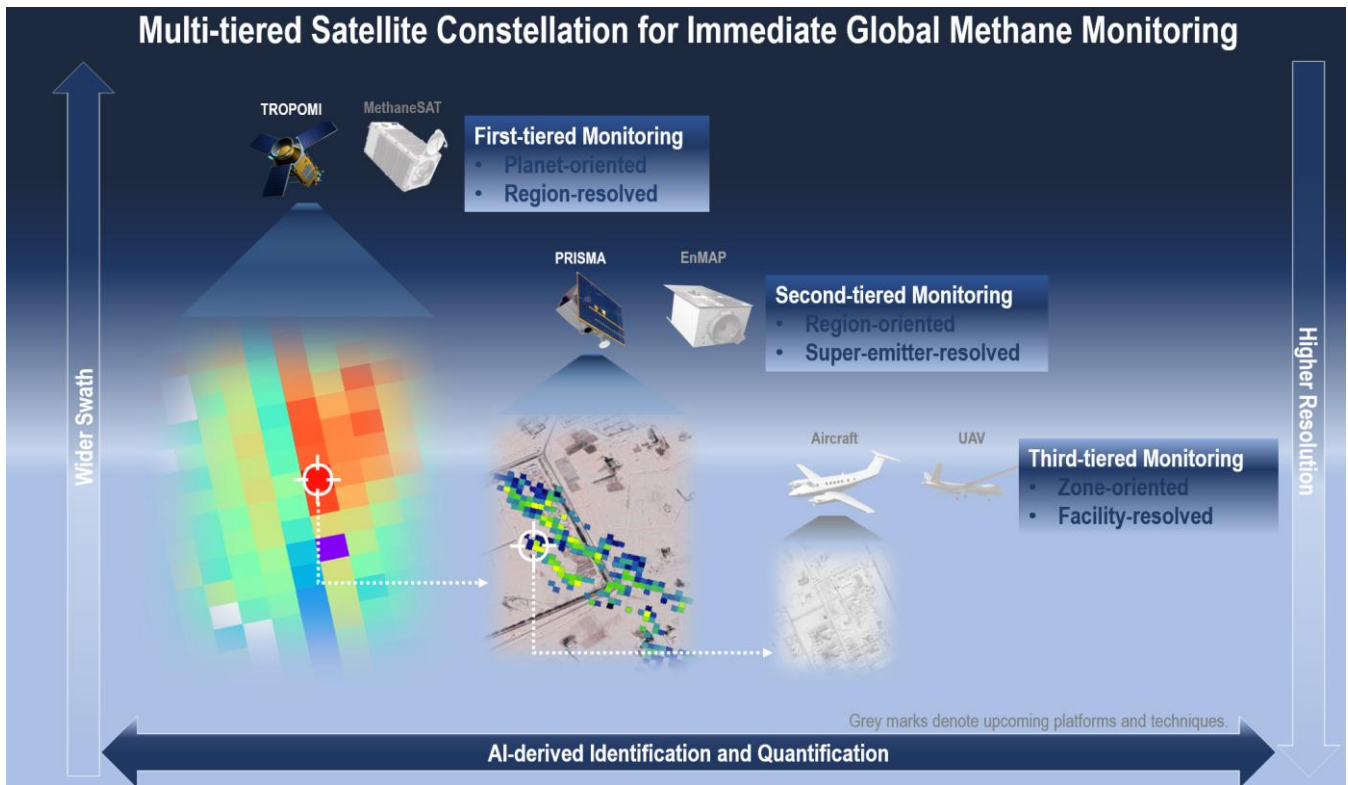
474

475 **Fig. 3. Comparison of emission estimates of methane plumes between surveys.** The surveys for the California field and
 476 Permian basin are selected as the references. They report 1181 and 39 methane plumes, while our second-tiered survey attempts
 477 29 plumes. Violin plots show statistical distributions of methane plume emission rates for these surveys. For each survey, the
 478 grey dots refer to the emission rates of the individual plumes and the red dot represents the median value.



479

480 **Fig. 4. Multi-tiered emission estimates versus bottom-up emission inventories.** We first interpolate the bottom-up emission
 481 inventories into the resolution consistent with our multi-tiered results. On this basis, the bottom-up emission rates in the grids
 482 that the detected hotspots and plumes cover are summed up to compare with the results. The detected hotspots (yellow dots)
 483 and plumes (blue dots) correspond to those as shown in Fig. 1. The grey dashed line represents the ratio of the bottom-up
 484 emissions to the top-down ones of 1:1.



485

486 **Fig. 5. Multi-tiered satellite framework for immediate global methane monitoring.** This framework harmonizes global-
 487 scale and high-resolution methane retrievals, with a dual focus on mapping region-scale and plant-level drivers. In this work,
 488 the framework reconciles the spacious swath of TROPOMI (i.e., ~ 2600 km) with the high resolution of PRISMA (i.e., 30 ×
 489 30 m²), in contrast to conventional satellite-based surveys that were of either insufficient samplings or narrow views. Looking
 490 forward, developments of Earth’s monitoring platforms (e.g., satellites, aircrafts, and unmanned drones) and artificial
 491 intelligence will continue to strengthen the performance of methane plume retrievals and emission estimates. On eve of the
 492 Paris target, at least while a super methane satellite with spacious swath, high resolution, and agile analysis is not in place, our
 493 multi-tiered satellite constellation has important implications for measuring global methane pledges. The appearances of the
 494 TROPOMI, MethaneSAT, PRISMA, and EnMAP are obtained from <http://www.tropomi.eu/>, <https://www.methanesat.org>,
 495 <https://www.asi.it/en/earth-science/prisma/>, and <https://www.enmap.org/>, respectively. The methane maps from the
 496 TROPOMI and PRISMA refer to the results in Figs. 1e and 1b1. The grey marks indicate upcoming platforms (i.e.,
 497 MethaneSAT and EnMAP) and techniques (e.g., AI techniques that can optimize the identification and quantification of
 498 methane super-emitters).

500 **Table 1. Spaceborne measurements for global methane monitoring.**

Satellite	Coverage/ Swath	Pixel Size (km ²)	SWIR (nm)	Spectral Resolution (nm)	Overpass (Local Time)	Period	Reference
SCIAMACHY	960 km	30 × 60	1630–1670	1.4	10:00	2002–2012	(Frankenberg et al., 2006)
GOSAT	790 km	10 × 10	1630–1700	0.06	13:00	2009–present	(Kuze et al., 2016)
GOSAT-2	1000 km	10 × 10	1630–1700, 2330–2380	0.06	13:00	2018–present	(Suto et al., 2021)
TROPOMI	2600 km	5.5 × 7, 7 × 7	2305–2385	0.25	13:30	2017–present	(Butz et al., 2012)
Sentinel-3	1420 km	0.5 × 0.5	1580–1640, 2230–2280	0.025	10:00	2016–present	(Pandey et al., 2022)
GHGSat	12 × 12 km ²	0.05 × 0.05	1600–1700	0.3–0.7	9:30	2016–present	(Varon et al., 2018)
PRISMA	30 × 30 km ²	0.03 × 0.03	1600–1700, 2200–2500	10	10:30	2019–present	(Guanter et al., 2021)
GF-5	60 × 60 km ²	0.03 × 0.03	2100–2400	10	13:30	2018–present	(Irakulis-Loitxate et al., 2022)
ZY1	60 × 60 km ²	0.03 × 0.03	2100–2400	10	10:50		(Irakulis-Loitxate et al., 2022)
Landsat-8	185 × 185 km ²	0.03 × 0.03	2300	200	10:50	2013–present	(Ehret et al., 2022)
Sentinel-2	290 km	0.02 × 0.02	1610, 2190	200	10:30	2015–present	(Varon et al., 2021)
Worldview-3	66.5 × 112 km ²	0.0037 × 0.0037	2295–2365	50	10:30	2014–present	(Sánchez-García et al., 2021)
EnMAP	30 × 30 km ²	0.03 × 0.03	1600–1700, 2200–2450	10	11:00	2020–present	(Cusworth et al., 2019)
EMIT	80 km	0.06 × 0.06	1600–1700, 2200–2510	7.4		2022–present	(EMIT, 2023)

502 **Data availability.**

503 The operational TROPOMI product is available at <https://scihub.copernicus.eu/>, <https://www.temis.nl/emissions/data.php>. The
504 PRISMA data are publicly available to registered users at <https://prisma.asi.it/>. The WRF-CHEM model code is available at
505 <https://ruc.noaa.gov/wrf/wrf-chem/>. All Sentinel-2 satellite data are publicly available through the Copernicus Open Access
506 Hub (<https://scihub.copernicus.eu/>). The HITRAN line spectra is publicly available through the HITRANonline database
507 (<https://hitran.org/>). The ERA5 data come from <https://www.ecmwf.int/en/forecasts/datasets/reanalysis-datasets/era5>. The
508 EDGARv6.0 dataset comes from <https://edgar.jrc.ec.europa.eu/gallery?release=v60ghg&substance=CH4§or=TOTALS>.

509 **Code availability.**

510 The codes are available upon request to corresponding author.

511 **Supplementary information.**

512 Supplementary information accompanies this paper.

513 **Author contributions.**

514 P. L. designed this study and wrote the manuscript. P. L. and Y. W. developed the retrieval algorithm. P. L., Y. W., X. G., Y.
515 H., and Y. P. performed the data analysis. S. Y., A.B., D. R., and J. H. S. contributed to the manuscript.

516 **Competing interests.**

517 The authors declare no competing interests.

518 **Acknowledgements.**

519 We thank ESA and the S-5P/TROPOMI team for the great work on initiating and realizing TROPOMI data. We also thank
520 the Italian Space Agency for the great work on the PRISMA data. This study is funded by National Natural Science Foundation
521 of China (No. 22006030, 22076172, 21577126 and 41561144004), Science and Technology Program of Hebei Province
522 (22343702D), Science and Technology Project of Hebei Education Department (BJ2020032 and QN2019184), Basic Scientific
523 Research Foundation of Hebei (KY2021024), Initiation Fund of Hebei Agricultural University (412201904 and YJ201833),
524 the Department of Science and Technology of China (No. 2016YFC0202702, 2018YFC0213506 and 2018YFC0213503), and
525 National Research Program for Key Issues in Air Pollution Control in China (No. DQGG0107).

526 **References**

- 527 Allen, D. T., Torres, V. M., Thomas, J., Sullivan, D. W., Harrison, M., Hendler, A., Herndon, S. C., Kolb, C. E., Fraser, M.
528 P., Hill, A. D., Lamb, B. K., Miskimins, J., Sawyer, R. F. and Seinfeld, J. H.: Measurements of methane emissions at natural
529 gas production sites in the United States, *Proc. Natl. Acad. Sci.*, 110(44), 17768–17773, doi:10.1073/pnas.1304880110,
530 2013.
- 531 Allen, F., Gokul, I., Leon, C., James, E., Nathan, H., Haewon, M., Joeri, R., Reed, S., Jameel, A., R., A. G., Jared, C., Minji,
532 J., James, M., Anupriya, M. and Wenjing, S.: Can Paris pledges avert severe climate change?, *Science* (80-.), 350(6265),
533 1168–1169, doi:10.1126/science.aad5761, 2015.
- 534 Alvarez, R. A., Zavala-Araiza, D., Lyon, D. R., Allen, D. T., Barkley, Z. R., Brandt, A. R., Davis, K. J., Herndon, S. C.,
535 Jacob, D. J. and Karion, A.: Assessment of methane emissions from the US oil and gas supply chain, *Science* (80-.),
536 361(6398), 186–188, 2018.
- 537 Butz, A., Hasekamp, O. P., Frankenberg, C. and Aben, I.: Retrievals of atmospheric CO₂ from simulated space-borne
538 measurements of backscattered near-infrared sunlight: accounting for aerosol effects, *Appl. Opt.*, 48(18), 3322–3336,
539 doi:10.1364/AO.48.003322, 2009.
- 540 Butz, A., Guerlet, S., Hasekamp, O., Schepers, D., Galli, A., Aben, I., Frankenberg, C., Hartmann, J.-M., Tran, H., Kuze, A.,
541 Keppel-Aleks, G., Toon, G., Wunch, D., Wennberg, P., Deutscher, N., Griffith, D., Macatangay, R., Messerschmidt, J.,
542 Notholt, J. and Warneke, T.: Toward accurate CO₂ and CH₄ observations from GOSAT, *Geophys. Res. Lett.*, 38(14),
543 doi:https://doi.org/10.1029/2011GL047888, 2011.
- 544 Butz, A., Galli, A., Hasekamp, O., Landgraf, J., Tol, P. and Aben, I.: TROPOMI aboard Sentinel-5 Precursor: Prospective
545 performance of CH₄ retrievals for aerosol and cirrus loaded atmospheres, *Remote Sens. Environ.*, 120, 267–276,
546 doi:https://doi.org/10.1016/j.rse.2011.05.030, 2012.
- 547 Conley, S., Franco, G., Faloon, I., Blake, D. R., Peischl, J. and Ryerson, T. B.: Methane emissions from the 2015 Aliso
548 Canyon blowout in Los Angeles, CA, *Science* (80-.), 351(6279), 1317–1320, 2016.
- 549 Crippa, M., Solazzo, E., Huang, G., Guizzardi, D., Koffi, E., Muntean, M., Schieberle, C., Friedrich, R. and Janssens-
550 Maenhout, G.: High resolution temporal profiles in the Emissions Database for Global Atmospheric Research, *Sci. Data*,
551 7(1), 121, doi:10.1038/s41597-020-0462-2, 2020.
- 552 Cusworth, D. H., Jacob, D. J., Varon, D. J., Chan Miller, C., Liu, X., Chance, K., Thorpe, A. K., Duren, R. M., Miller, C. E.,
553 Thompson, D. R., Frankenberg, C., Guanter, L. and Randles, C. A.: Potential of next-generation imaging spectrometers to
554 detect and quantify methane point sources from space, *Atmos. Meas. Tech.*, 12(10), 5655–5668, doi:10.5194/amt-12-5655-
555 2019, 2019.
- 556 Cusworth, D. H., Duren, R. M., Yadav, V., Thorpe, A. K., Verhulst, K., Sander, S., Hopkins, F., Rafiq, T. and Miller, C. E.:
557 Synthesis of Methane Observations Across Scales: Strategies for Deploying a Multitiered Observing Network, *Geophys.*
558 *Res. Lett.*, 47(7), e2020GL087869, doi:https://doi.org/10.1029/2020GL087869, 2020.

559 Cusworth, D. H., Duren, R. M., Thorpe, A. K., Olson-Duvall, W., Heckler, J., Chapman, J. W., Eastwood, M. L.,
560 Helmlinger, M. C., Green, R. O., Asner, G. P., Dennison, P. E. and Miller, C. E.: Intermittency of Large Methane Emitters in
561 the Permian Basin, *Environ. Sci. Technol. Lett.*, 8(7), 567–573, doi:10.1021/acs.estlett.1c00173, 2021a.

562 Cusworth, D. H., Duren, R. M., Thorpe, A. K., Pandey, S., Maasackers, J. D., Aben, I., Jervis, D., Varon, D. J., Jacob, D. J.
563 and Randles, C. A.: Multisatellite Imaging of a Gas Well Blowout Enables Quantification of Total Methane Emissions,
564 *Geophys. Res. Lett.*, 48(2), e2020GL090864, 2021b.

565 Deng, Z., Ciais, P., Tzompa-Sosa, Z. A., Saunois, M., Qiu, C., Tan, C., Sun, T., Ke, P., Cui, Y., Tanaka, K., Lin, X.,
566 Thompson, R. L., Tian, H., Yao, Y., Huang, Y., Lauerwald, R., Jain, A. K., Xu, X., Bastos, A., Sitch, S., Palmer, P. I.,
567 Lauvaux, T., d'Aspremont, A., Giron, C., Benoit, A., Poulter, B., Chang, J., Petrescu, A. M. R., Davis, S. J., Liu, Z., Grassi,
568 G., Albergel, C., Tubiello, F. N., Perugini, L., Peters, W. and Chevallier, F.: Comparing national greenhouse gas budgets
569 reported in UNFCCC inventories against atmospheric inversions, *Earth Syst. Sci. Data*, 14(4), 1639–1675, doi:10.5194/essd-
570 14-1639-2022, 2022.

571 Duren, R. M., Thorpe, A. K., Foster, K. T., Rafiq, T., Hopkins, F. M., Yadav, V., Bue, B. D., Thompson, D. R., Conley, S.
572 and Colombi, N. K.: California's methane super-emitters, *Nature*, 575(7781), 180–184, 2019.

573 Ehret, T., Truchis, A. De, Mazzolini, M., Morel, J.-M., d'Aspremont, A., Lauvaux, T., Duren, R., Cusworth, D. and
574 Facciolo, G.: Global Tracking and Quantification of Oil and Gas Methane Emissions from Recurrent Sentinel-2 Imagery,
575 2021.

576 Ehret, T., De Truchis, A., Mazzolini, M., Morel, J.-M., d'Aspremont, A., Lauvaux, T., Duren, R., Cusworth, D. and
577 Facciolo, G.: Global Tracking and Quantification of Oil and Gas Methane Emissions from Recurrent Sentinel-2 Imagery,
578 *Environ. Sci. Technol.*, 56(14), 10517–10529, doi:10.1021/acs.est.1c08575, 2022.

579 EMIT: Earth Surface Mineral Dust Source Investigation (EMIT), [online] Available from: <https://earth.jpl.nasa.gov/emit/>,
580 2023.

581 Englander, J. G., Brandt, A. R., Conley, S., Lyon, D. R. and Jackson, R. B.: Aerial Interyear Comparison and Quantification
582 of Methane Emissions Persistence in the Bakken Formation of North Dakota, USA, *Environ. Sci. Technol.*, 52(15), 8947–
583 8953, doi:10.1021/acs.est.8b01665, 2018.

584 Etminan, M., Myhre, G., Highwood, E. J. and Shine, K. P.: Radiative forcing of carbon dioxide, methane, and nitrous oxide:
585 A significant revision of the methane radiative forcing, *Geophys. Res. Lett.*, 43(24), 12,612–614,623,
586 doi:<https://doi.org/10.1002/2016GL071930>, 2016.

587 Foote, M. D., Dennison, P. E., Thorpe, A. K., Thompson, D. R., Jongaramrungruang, S., Frankenberg, C. and Joshi, S. C.:
588 Fast and Accurate Retrieval of Methane Concentration From Imaging Spectrometer Data Using Sparsity Prior, *IEEE Trans.*
589 *Geosci. Remote Sens.*, 58(9), 6480–6492, doi:10.1109/TGRS.2020.2976888, 2020.

590 Frankenberg, C., Meirink, J. F., Bergamaschi, P., Goede, A. P. H., Heimann, M., Körner, S., Platt, U., van Weele, M. and
591 Wagner, T.: Satellite cartography of atmospheric methane from SCIAMACHY on board ENVISAT: Analysis of the years
592 2003 and 2004, *J. Geophys. Res. Atmos.*, 111(D7), doi:<https://doi.org/10.1029/2005JD006235>, 2006.

593 Frankenberg, C., Thorpe, A. K., Thompson, D. R., Hulley, G., Kort, E. A., Vance, N., Borchardt, J., Krings, T., Gerilowski,
594 K., Sweeney, C., Conley, S., Bue, B. D., Aubrey, A. D., Hook, S. and Green, R. O.: Airborne methane remote measurements
595 reveal heavy-tail flux distribution in Four Corners region, *Proc. Natl. Acad. Sci.*, 113(35), 9734 LP – 9739,
596 doi:10.1073/pnas.1605617113, 2016.

597 Gålfalk, M., Nilsson Påledal, S. and Bastviken, D.: Sensitive Drone Mapping of Methane Emissions without the Need for
598 Supplementary Ground-Based Measurements, *ACS Earth Sp. Chem.*, 5(10), 2668–2676,
599 doi:10.1021/acsearthspacechem.1c00106, 2021.

600 Ganesan, A. L., Schwietzke, S., Poulter, B., Arnold, T., Lan, X., Rigby, M., Vogel, F. R., van der Werf, G. R., Janssens-
601 Maenhout, G., Boesch, H., Pandey, S., Manning, A. J., Jackson, R. B., Nisbet, E. G. and Manning, M. R.: Advancing
602 Scientific Understanding of the Global Methane Budget in Support of the Paris Agreement, *Global Biogeochem. Cycles*,
603 33(12), 1475–1512, doi:https://doi.org/10.1029/2018GB006065, 2019.

604 Guanter, L., Irakulis-Loitxate, I., Gorroño, J., Sánchez-García, E., Cusworth, D. H., Varon, D. J., Cogliati, S. and Colombo,
605 R.: Mapping methane point emissions with the PRISMA spaceborne imaging spectrometer, *Remote Sens. Environ.*, 265,
606 112671, doi:https://doi.org/10.1016/j.rse.2021.112671, 2021.

607 Hasekamp, O. P. and Butz, A.: Efficient calculation of intensity and polarization spectra in vertically inhomogeneous
608 scattering and absorbing atmospheres, *J. Geophys. Res. Atmos.*, 113(D20), doi:https://doi.org/10.1029/2008JD010379, 2008.

609 Hoffmann, L., Günther, G., Li, D., Stein, O., Wu, X., Griessbach, S., Heng, Y., Konopka, P., Müller, R., Vogel, B. and
610 Wright, J. S.: From ERA-Interim to ERA5: the considerable impact of ECMWF's next-generation reanalysis on Lagrangian
611 transport simulations, *Atmos. Chem. Phys.*, 19(5), 3097–3124, doi:10.5194/acp-19-3097-2019, 2019.

612 Hu, H., Landgraf, J., Detmers, R., Borsdorff, T., Aan de Brugh, J., Aben, I., Butz, A. and Hasekamp, O.: Toward Global
613 Mapping of Methane With TROPOMI: First Results and Intersatellite Comparison to GOSAT, *Geophys. Res. Lett.*, 45(8),
614 3682–3689, doi:https://doi.org/10.1002/2018GL077259, 2018.

615 Irakulis-Loitxate, I., Guanter, L., Liu, Y.-N., Varon, D. J., Maasackers, J. D., Zhang, Y., Chulakadabba, A., Wofsy, S. C.,
616 Thorpe, A. K., Duren, R. M. and Others: Satellite-based survey of extreme methane emissions in the Permian basin, *Sci.*
617 *Adv.*, 7(27), eabf4507, doi:10.1126/sciadv.abf4507, 2022.

618 Itziar, I.-L., Luis, G., Yin-Nian, L., J., V. D., D., M. J., Yuzhong, Z., Apisada, C., C., W. S., K., T. A., M., D. R., Christian,
619 F., R., L. D., Benjamin, H., H., C. D., Yongguang, Z., Karl, S., Javier, G., Elena, S.-G., P., S. M., Kaiqin, C., Haijian, Z.,
620 Jian, L., Xun, L., Ilse, A. and J., J. D.: Satellite-based survey of extreme methane emissions in the Permian basin, *Sci. Adv.*,
621 7(27), eabf4507, doi:10.1126/sciadv.abf4507, 2021.

622 Jacob, D. J., Turner, A. J., Maasackers, J. D., Sheng, J., Sun, K., Liu, X., Chance, K., Aben, I., McKeever, J. and
623 Frankenberg, C.: Satellite observations of atmospheric methane and their value for quantifying methane emissions, *Atmos.*
624 *Chem. Phys.*, 16(22), 14371–14396, doi:10.5194/acp-16-14371-2016, 2016.

625 Jervis, D., McKeever, J., Durak, B. O. A., Sloan, J. J., Gains, D., Varon, D. J., Ramier, A., Strupler, M. and Tarrant, E.: The
626 GHGSat-D imaging spectrometer, *Atmos. Meas. Tech.*, 14(3), 2127–2140, doi:10.5194/amt-14-2127-2021, 2021.

627 Kraut, S., Scharf, L. L. and Butler, R. W.: The adaptive coherence estimator: a uniformly most-powerful-invariant adaptive
628 detection statistic, *IEEE Trans. Signal Process.*, 53(2), 427–438, doi:10.1109/TSP.2004.840823, 2005.

629 Kuze, A., Suto, H., Shiomi, K., Kawakami, S., Tanaka, M., Ueda, Y., Deguchi, A., Yoshida, J., Yamamoto, Y., Kataoka, F.,
630 Taylor, T. E. and Buijs, H. L.: Update on GOSAT TANSO-FTS performance, operations, and data products after more than
631 6 years in space, *Atmos. Meas. Tech.*, 9(6), 2445–2461, doi:10.5194/amt-9-2445-2016, 2016.

632 Lauvaux, T., Giron, C., Mazzolini, M., d’Aspremont, A., Duren, R., Cusworth, D., Shindell, D. and Ciais, P.: Global
633 assessment of oil and gas methane ultra-emitters, *Science (80-.)*, 375(6580), 557–561, 2022.

634 Lorente, A., Borsdorff, T., Butz, A., Hasekamp, O., aan de Brugh, J., Schneider, A., Wu, L., Hase, F., Kivi, R., Wunch, D.,
635 Pollard, D. F., Shiomi, K., Deutscher, N. M., Velazco, V. A., Roehl, C. M., Wennberg, P. O., Warneke, T. and Landgraf, J.:
636 Methane retrieved from TROPOMI: improvement of the data product and validation of the first 2 years of measurements,
637 *Atmos. Meas. Tech.*, 14(1), 665–684, doi:10.5194/amt-14-665-2021, 2021.

638 Maasackers, J. D., Varon, D. J., Elfarsdóttir, A., McKeever, J., Jervis, D., Mahapatra, G., Pandey, S., Lorente, A., Borsdorff,
639 T., Foothuis, L. R., Schuit, B. J., Tol, P., van Kempen, T. A., van Hees, R. and Aben, I.: Using satellites to uncover large
640 methane emissions from landfills, *Sci. Adv.*, 8(32), eabn9683, doi:10.1126/sciadv.abn9683, 2023.

641 Marchese, A. J., Vaughn, T. L., Zimmerle, D. J., Martinez, D. M., Williams, L. L., Robinson, A. L., Mitchell, A. L.,
642 Subramanian, R., Tkacik, D. S., Roscioli, J. R. and Herndon, S. C.: Methane Emissions from United States Natural Gas
643 Gathering and Processing, *Environ. Sci. Technol.*, 49(17), 10718–10727, doi:10.1021/acs.est.5b02275, 2015.

644 Martin, Van, Damme, Lieven, Clarisse, Simon, Whitburn, Juliette, Hadji-Lazaro and Daniel: Industrial and agricultural
645 ammonia point sources exposed, *Nature*, 2018.

646 Masood, E. and Tollefson, J.: COP26 climate pledges: What scientists think so far, *Nature*, d41586-021-03034-z,
647 doi:10.1038/d41586-021-03034-z, 2021.

648 Mayfield, E. N., Robinson, A. L. and Cohon, J. L.: System-wide and Superemitter Policy Options for the Abatement of
649 Methane Emissions from the U.S. Natural Gas System, *Environ. Sci. Technol.*, 51(9), 4772–4780,
650 doi:10.1021/acs.est.6b05052, 2017.

651 Mikaloff, F. S. E. and Hinrich, S.: Rising methane: A new climate challenge, *Science (80-.)*, 364(6444), 932–933,
652 doi:10.1126/science.aax1828, 2019.

653 Miller, S. M., Michalak, A. M., Detmers, R. G., Hasekamp, O. P., Bruhwiler, L. M. P. and Schwietzke, S.: China’s coal mine
654 methane regulations have not curbed growing emissions, *Nat. Commun.*, 10(1), 1–8, 2019.

655 National Oceanic and Atmospheric Administration: Increase in atmospheric methane set another record during 2021,
656 [online] Available from: [https://www.noaa.gov/news-release/increase-in-atmospheric-methane-set-another-record-during-](https://www.noaa.gov/news-release/increase-in-atmospheric-methane-set-another-record-during-2021)
657 2021, 2022.

658 Nisbet, E. G., Dlugokencky, E. J. and Bousquet, P.: Methane on the Rise—Again, *Science (80-.)*, 343(6170), 493–495,
659 doi:10.1126/science.1247828, 2014.

660 Nisbet, E. G., Manning, M. R., Dlugokencky, E. J., Fisher, R. E., Lowry, D., Michel, S. E., Myhre, C. L., Platt, S. M., Allen,
661 G. and Bousquet, P.: Very Strong Atmospheric Methane Growth in the 4Years 2014–2017: Implications for the Paris
662 Agreement, *Global Biogeochem. Cycles*, 33, 2019.

663 Nisbet, E. G., Fisher, R. E., Lowry, D., France, J. L., Allen, G., Bakkaloglu, S., Broderick, T. J., Cain, M., Coleman, M.,
664 Fernandez, J., Forster, G., Griffiths, P. T., Iverach, C. P., Kelly, B. F. J., Manning, M. R., Nisbet-Jones, P. B. R., Pyle, J. A.,
665 Townsend-Small, A., al-Shalaan, A., Warwick, N. and Zazzeri, G.: Methane Mitigation: Methods to Reduce Emissions, on
666 the Path to the Paris Agreement, *Rev. Geophys.*, 58(1), e2019RG000675, doi:<https://doi.org/10.1029/2019RG000675>, 2020.

667 Ocko, I. B., Sun, T., Shindell, D., Oppenheimer, M., Hristov, A. N., Pacala, S. W., Mauzerall, D. L., Xu, Y. and Hamburg, S.
668 P.: Acting rapidly to deploy readily available methane mitigation measures by sector can immediately slow global warming,
669 *Environ. Res. Lett.*, 16(5), 54042, doi:10.1088/1748-9326/abf9c8, 2021.

670 Ouerghi, E., Ehret, T., de Franchis, C., Facciolo, G., Lauvaux, T., Meinhardt, E. and Morel, J.-M.: Detection of methane
671 plumes in hyperspectral images from SENTINEL-5P by coupling anomaly detection and pattern recognition, *ISPRS Ann.*
672 *Photogramm. Remote Sens. Spat. Inf. Sci.*, V-3–2021, 81–87, doi:10.5194/isprs-annals-V-3-2021-81-2021, 2021.

673 Pandey, S., Gautam, R., Houweling, S., Van Der Gon, H. D., Sadavarte, P., Borsdorff, T., Hasekamp, O., Landgraf, J., Tol,
674 P. and Van Kempen, T.: Satellite observations reveal extreme methane leakage from a natural gas well blowout, *Proc. Natl.*
675 *Acad. Sci.*, 116(52), 26376–26381, 2019.

676 Pandey, S., Houweling, S., Lorente, A., Borsdorff, T., Tsiavidou, M., Bloom, A. A., Poulter, B., Zhang, Z. and Aben, I.:
677 Using satellite data to identify the methane emission controls of South Sudan’s wetlands, *Biogeosciences*, 18(2), 557–572,
678 doi:10.5194/bg-18-557-2021, 2021.

679 Pandey, S., van Nistelrooij, M., Maasackers, J. D., Sutar, P., Houweling, S., Varon, D. J., Tol, P., Gains, D., Worden, J. and
680 Aben, I.: Daily detection and quantification of methane leaks using Sentinel-3: a tiered satellite observation approach with
681 Sentinel-2 and Sentinel-5p, , doi:10.48550/ARXIV.2212.11318, 2022.

682 Paoletti, M. E., Haut, J. M., Plaza, J. and Plaza, A.: A new deep convolutional neural network for fast hyperspectral image
683 classification, *ISPRS J. Photogramm. Remote Sens.*, 145, 120–147, doi:<https://doi.org/10.1016/j.isprsjprs.2017.11.021>, 2018.

684 Phil DeCola and WMO Secretariat: An Integrated Global Greenhouse Gas Information System (IG3IS), [online] Available
685 from: <https://public.wmo.int/en/resources/bulletin/integrated-global-greenhouse-gas-information-system-ig3is>, 2017.

686 Plant, G., Kort, E. A., Brandt, A. R., Chen, Y., Fordice, G., Gorchov Negron, A. M., Schwietzke, S., Smith, M. and Zavala-
687 Araiza, D.: Inefficient and unlit natural gas flares both emit large quantities of methane, *Science* (80-.), 377(6614), 1566–
688 1571, doi:10.1126/science.abq0385, 2022.

689 Poindexter, C. M., Baldocchi, D. D., Matthes, J. H., Knox, S. H. and Variano, E. A.: The contribution of an overlooked
690 transport process to a wetland’s methane emissions, *Geophys. Res. Lett.*, 43(12), 6276–6284,
691 doi:<https://doi.org/10.1002/2016GL068782>, 2016.

692 Reichstein, M., Camps-Valls, G., Stevens, B., Jung, M., Denzler, J., Carvalhais, N. and Prabhat: Deep learning and process
693 understanding for data-driven Earth system science, *Nature*, 566(7743), 195–204, doi:10.1038/s41586-019-0912-1, 2019.

694 Sadavarte, P., Pandey, S., Maasackers, J. D., Lorente, A., Borsdorff, T., Denier van der Gon, H., Houweling, S. and Aben, I.:
695 Methane Emissions from Superemitting Coal Mines in Australia Quantified Using TROPOMI Satellite Observations,
696 *Environ. Sci. Technol.*, 55(24), 16573–16580, doi:10.1021/acs.est.1c03976, 2021.

697 Sánchez-García, E., Gorroño, J., Irakulis-Loitxate, I., Varon, D. J. and Guanter, L.: Mapping methane plumes at very high
698 spatial resolution with the WorldView-3 satellite, *Atmos. Meas. Tech. Discuss.*, 2021, 1–26, doi:10.5194/amt-2021-238,
699 2021.

700 Saunio, M., Bousquet, P., Poulter, B., Peregón, A., Ciais, P., Canadell, J. G., Dlugokencky, E. J., Etiope, G., Bastviken, D.,
701 Houweling, S., Janssens-Maenhout, G., Tubiello, F. N., Castaldi, S., Jackson, R. B., Alexe, M., Arora, V. K., Beerling, D. J.,
702 Bergamaschi, P., Blake, D. R., Brailsford, G., Brovkin, V., Bruhwiler, L., Crevoisier, C., Crill, P., Covey, K., Curry, C.,
703 Frankenberg, C., Gedney, N., Höglund-Isaksson, L., Ishizawa, M., Ito, A., Joos, F., Kim, H.-S., Kleinen, T., Krummel, P.,
704 Lamarque, J.-F., Langenfelds, R., Locatelli, R., Machida, T., Maksyutov, S., McDonald, K. C., Marshall, J., Melton, J. R.,
705 Morino, I., Naik, V., O’Doherty, S., Parmentier, F.-J. W., Patra, P. K., Peng, C., Peng, S., Peters, G. P., Pison, I., Prigent, C.,
706 Prinn, R., Ramonet, M., Riley, W. J., Saito, M., Santini, M., Schroeder, R., Simpson, I. J., Spahni, R., Steele, P., Takizawa,
707 A., Thornton, B. F., Tian, H., Tohjima, Y., Viovy, N., Voulgarakis, A., van Weele, M., van der Werf, G. R., Weiss, R.,
708 Wiedinmyer, C., Wilton, D. J., Wiltshire, A., Worthy, D., Wunch, D., Xu, X., Yoshida, Y., Zhang, B., Zhang, Z. and Zhu,
709 Q.: The global methane budget 2000–2012, *Earth Syst. Sci. Data*, 8(2), 697–751, doi:10.5194/essd-8-697-2016, 2016.

710 Saunio, M., Stavert, A. R., Poulter, B., Bousquet, P., Canadell, J. G., Jackson, R. B., Raymond, P. A., Dlugokencky, E. J.,
711 Houweling, S., Patra, P. K., Ciais, P., Arora, V. K., Bastviken, D., Bergamaschi, P., Blake, D. R., Brailsford, G., Bruhwiler,
712 L., Carlson, K. M., Carrol, M., Castaldi, S., Chandra, N., Crevoisier, C., Crill, P. M., Covey, K., Curry, C. L., Etiope, G.,
713 Frankenberg, C., Gedney, N., Hegglin, M. I., Höglund-Isaksson, L., Hugelius, G., Ishizawa, M., Ito, A., Janssens-Maenhout,
714 G., Jensen, K. M., Joos, F., Kleinen, T., Krummel, P. B., Langenfelds, R. L., Laruelle, G. G., Liu, L., Machida, T.,
715 Maksyutov, S., McDonald, K. C., McNorton, J., Miller, P. A., Melton, J. R., Morino, I., Müller, J., Murguía-Flores, F., Naik,
716 V., Niwa, Y., Noce, S., O’Doherty, S., Parker, R. J., Peng, C., Peng, S., Peters, G. P., Prigent, C., Prinn, R., Ramonet, M.,
717 Regnier, P., Riley, W. J., Rosentreter, J. A., Segers, A., Simpson, I. J., Shi, H., Smith, S. J., Steele, L. P., Thornton, B. F.,
718 Tian, H., Tohjima, Y., Tubiello, F. N., Tsuruta, A., Viovy, N., Voulgarakis, A., Weber, T. S., van Weele, M., van der Werf,
719 G. R., Weiss, R. F., Worthy, D., Wunch, D., Yin, Y., Yoshida, Y., Zhang, W., Zhang, Z., Zhao, Y., Zheng, B., Zhu, Q., Zhu,
720 Q. and Zhuang, Q.: The Global Methane Budget 2000–2017, *Earth Syst. Sci. Data*, 12(3), 1561–1623, doi:10.5194/essd-12-
721 1561-2020, 2020.

722 Schellnhuber, H. J., Rahmstorf, S. and Winkelmann, R.: Why the right climate target was agreed in Paris, *Nat. Clim. Chang.*,
723 6(7), 649–653, doi:10.1038/nclimate3013, 2016.

724 Schurer, A. P., Cowtan, K., Hawkins, E., Mann, M. E., Scott, V. and Tett, S. F. B.: Interpretations of the Paris climate target,
725 *Nat. Geosci.*, 11(4), 220–221, doi:10.1038/s41561-018-0086-8, 2018.

726 Sha, M. K., Langerock, B., Blavier, J.-F. L., Blumenstock, T., Borsdorff, T., Buschmann, M., Dehn, A., De Mazière, M.,
727 Deutscher, N. M., Feist, D. G., García, O. E., Griffith, D. W. T., Grutter, M., Hannigan, J. W., Hase, F., Heikkinen, P.,

728 Hermans, C., Iraci, L. T., Jeseck, P., Jones, N., Kivi, R., Kumps, N., Landgraf, J., Lorente, A., Mahieu, E., Makarova, M. V,
729 Mellqvist, J., Metzger, J.-M., Morino, I., Nagahama, T., Notholt, J., Ohyama, H., Ortega, I., Palm, M., Petri, C., Pollard, D.
730 F., Rettinger, M., Robinson, J., Roche, S., Roehl, C. M., Röhling, A. N., Rousogonous, C., Schneider, M., Shiomi, K., Smale,
731 D., Stremme, W., Strong, K., Sussmann, R., Té, Y., Uchino, O., Velazco, V. A., Vigouroux, C., Vrekoussis, M., Wang, P.,
732 Warneke, T., Wizenberg, T., Wunch, D., Yamanouchi, S., Yang, Y. and Zhou, M.: Validation of methane and carbon
733 monoxide from Sentinel-5 Precursor using TCCON and NDACC-IRWG stations, *Atmos. Meas. Tech.*, 14(9), 6249–6304,
734 doi:10.5194/amt-14-6249-2021, 2021.

735 Shoemaker, J. K., Schrag, D. P., Molina, M. J. and Ramanathan, V.: What role for short-lived climate pollutants in
736 mitigation policy?, *Science* (80-.), 342(6164), 1323–1324, 2013.

737 Smith, M. L., Gvakharia, A., Kort, E. A., Sweeney, C., Conley, S. A., Faloona, I., Newberger, T., Schnell, R., Schwietzke, S.
738 and Wolter, S.: Airborne Quantification of Methane Emissions over the Four Corners Region, *Environ. Sci. Technol.*,
739 51(10), 5832–5837, doi:10.1021/acs.est.6b06107, 2017.

740 Subramanian, R., Williams, L. L., Vaughn, T. L., Zimmerle, D., Roscioli, J. R., Herndon, S. C., Yacovitch, T. I.,
741 Floerchinger, C., Tkacik, D. S., Mitchell, A. L., Sullivan, M. R., Dallmann, T. R. and Robinson, A. L.: Methane Emissions
742 from Natural Gas Compressor Stations in the Transmission and Storage Sector: Measurements and Comparisons with the
743 EPA Greenhouse Gas Reporting Program Protocol, *Environ. Sci. Technol.*, 49(5), 3252–3261, doi:10.1021/es5060258, 2015.

744 Suto, H., Kataoka, F., Kikuchi, N., Knuteson, R. O., Butz, A., Haun, M., Buijs, H., Shiomi, K., Imai, H. and Kuze, A.:
745 Thermal and near-infrared sensor for carbon observation Fourier transform spectrometer-2 (TANSO-FTS-2) on the
746 Greenhouse gases Observing SATellite-2 (GOSAT-2) during its first year in orbit, *Atmos. Meas. Tech.*, 14(3), 2013–2039,
747 doi:10.5194/amt-14-2013-2021, 2021.

748 The European Union’s Copernicus Climate Change Service: Annual summary 2021. [online] Available from:
749 [https://climate.copernicus.eu/sites/default/files/custom-uploads/Annual_summary_2021/C3S-CAMS annual temp data and](https://climate.copernicus.eu/sites/default/files/custom-uploads/Annual_summary_2021/C3S-CAMS_annual_temp_data_and_CO2_2021_press_release_final.pdf)
750 [CO2 2021_press release_final.pdf](https://climate.copernicus.eu/sites/default/files/custom-uploads/Annual_summary_2021/C3S-CAMS_annual_temp_data_and_CO2_2021_press_release_final.pdf), n.d.

751 Thompson, D. R., Thorpe, A. K., Frankenberg, C., Green, R. O., Duren, R., Guanter, L., Hollstein, A., Middleton, E., Ong,
752 L. and Ungar, S.: Space-based remote imaging spectroscopy of the Aliso Canyon CH₄ superemitter, *Geophys. Res. Lett.*,
753 43(12), 6571–6578, doi:<https://doi.org/10.1002/2016GL069079>, 2016.

754 Thorpe, A. K., Frankenberg, C., Aubrey, A. D., Roberts, D. A., Nottrott, A. A., Rahn, T. A., Sauer, J. A., Dubey, M. K.,
755 Costigan, K. R., Arata, C., Steffke, A. M., Hills, S., Haselwimmer, C., Charlesworth, D., Funk, C. C., Green, R. O.,
756 Lundeen, S. R., Boardman, J. W., Eastwood, M. L., Sarture, C. M., Nolte, S. H., Mccubbin, I. B., Thompson, D. R. and
757 McFadden, J. P.: Mapping methane concentrations from a controlled release experiment using the next generation airborne
758 visible/infrared imaging spectrometer (AVIRIS-NG), *Remote Sens. Environ.*, 179, 104–115,
759 doi:<https://doi.org/10.1016/j.rse.2016.03.032>, 2016.

760 Turner, A. J., Frankenberg, C. and Kort, E. A.: Interpreting contemporary trends in atmospheric methane, *Proc. Natl. Acad.*
761 *Sci.*, 116(8), 2805 LP – 2813, doi:10.1073/pnas.1814297116, 2019.

762 Tuzson, B., Graf, M., Ravelid, J., Scheidegger, P., Kupferschmid, A., Looser, H., Morales, R. P. and Emmenegger, L.: A
763 compact QCL spectrometer for mobile, high-precision methane sensing aboard drones, *Atmos. Meas. Tech.*, 13(9), 4715–
764 4726, doi:10.5194/amt-13-4715-2020, 2020.

765 United Nations: Global methane pledge, [online] Available from: [https://unfccc.int/news/world-leaders-kick-start-](https://unfccc.int/news/world-leaders-kick-start-accelerated-climate-action-at-cop26)
766 [accelerated-climate-action-at-cop26](https://unfccc.int/news/world-leaders-kick-start-accelerated-climate-action-at-cop26), 2021.

767 Varon, D., McKeever, J., Jervis, D., Maasackers, J. D., Pandey, S., Houweling, S., Aben, I., Scarpelli, T. and Jacob, D. J.:
768 Satellite Discovery of Anomalously Large Methane Point Sources From Oil/Gas Production, *Geophys. Res. Lett.*, 46,
769 doi:10.1029/2019GL083798, 2019.

770 Varon, D. J., Jacob, D. J., McKeever, J., Jervis, D., Durak, B. O. A., Xia, Y. and Huang, Y.: Quantifying methane point
771 sources from fine-scale satellite observations of atmospheric methane plumes, *Atmos. Meas. Tech.*, 11(10), 5673–5686,
772 doi:10.5194/amt-11-5673-2018, 2018.

773 Varon, D. J., Jacob, D. J., Jervis, D. and McKeever, J.: Quantifying Time-Averaged Methane Emissions from Individual
774 Coal Mine Vents with GHGSat-D Satellite Observations, *Environ. Sci. Technol.*, 54(16), 10246–10253,
775 doi:10.1021/acs.est.0c01213, 2020.

776 Varon, D. J., Jervis, D., McKeever, J., Spence, I., Gains, D. and Jacob, D. J.: High-frequency monitoring of anomalous
777 methane point sources with multispectral Sentinel-2 satellite observations, *Atmos. Meas. Tech.*, 14(4), 2771–2785,
778 doi:10.5194/amt-14-2771-2021, 2021.

779 Vaughn, T. L., Bell, C. S., Pickering, C. K., Schwietzke, S., Heath, G. A., Pétron, G., Zimmerle, D. J., Schnell, R. C. and
780 Nummedal, D.: Temporal variability largely explains top-down/bottom-up difference in methane emission estimates from a
781 natural gas production region, *Proc. Natl. Acad. Sci.*, 115(46), 11712–11717, 2018.

782 Veefkind, J. P., Aben, I., McMullan, K., Förster, H., de Vries, J., Otter, G., Claas, J., Eskes, H. J., de Haan, J. F., Kleipool,
783 Q., van Weele, M., Hasekamp, O., Hoogeveen, R., Landgraf, J., Snel, R., Tol, P., Ingmann, P., Voors, R., Kruizinga, B.,
784 Vink, R., Visser, H. and Levelt, P. F.: TROPOMI on the ESA Sentinel-5 Precursor: A GMES mission for global
785 observations of the atmospheric composition for climate, air quality and ozone layer applications, *Remote Sens. Environ.*,
786 120, 70–83, doi:<https://doi.org/10.1016/j.rse.2011.09.027>, 2012.

787 Verhoelst, T., Compernelle, S., Pinardi, G., Lambert, J.-C., Eskes, H. J., Eichmann, K.-U., Fjæraa, A. M., Granville, J.,
788 Niemeijer, S., Cede, A., Tiefengraber, M., Hendrick, F., Pazmiño, A., Bais, A., Bazureau, A., Boersma, K. F., Bogner, K.,
789 Dehn, A., Donner, S., Elokhov, A., Gebetsberger, M., Goutail, F., Grutter de la Mora, M., Gruzdev, A., Gratsea, M., Hansen,
790 G. H., Irie, H., Jepsen, N., Kanaya, Y., Karagkiozidis, D., Kivi, R., Kreher, K., Levelt, P. F., Liu, C., Müller, M., Navarro
791 Comas, M., Piders, A. J. M., Pommereau, J.-P., Portafaix, T., Prados-Roman, C., Puentedura, O., Querel, R., Remmers, J.,
792 Richter, A., Rimmer, J., Rivera Cárdenas, C., Saavedra de Miguel, L., Sinyakov, V. P., Stremme, W., Strong, K., Van
793 Roozendaal, M., Veefkind, J. P., Wagner, T., Wittrock, F., Yela González, M. and Zehner, C.: Ground-based validation of
794 the Copernicus Sentinel-5P TROPOMI NO₂ measurements with the NDACC ZSL-DOAS, MAX-DOAS and Pandonia
795 global networks, *Atmos. Meas. Tech.*, 14(1), 481–510, doi:10.5194/amt-14-481-2021, 2021.

796 World Meteorological Organization: Global Atmosphere Watch Programme (GAW), [online] Available from:
797 <https://community.wmo.int/activity-areas/gaw>, 2022.

798 Yang, X., Ye, Y., Li, X., Lau, R. Y. K., Zhang, X. and Huang, X.: Hyperspectral Image Classification With Deep Learning
799 Models, *IEEE Trans. Geosci. Remote Sens.*, 56(9), 5408–5423, doi:10.1109/TGRS.2018.2815613, 2018.

800 Yu, S., Jia, S. and Xu, C.: Convolutional neural networks for hyperspectral image classification, *Neurocomputing*, 219, 88–
801 98, doi:<https://doi.org/10.1016/j.neucom.2016.09.010>, 2017.

802 Yuan, Q., Shen, H., Li, T., Li, Z., Li, S., Jiang, Y., Xu, H., Tan, W., Yang, Q., Wang, J., Gao, J. and Zhang, L.: Deep
803 learning in environmental remote sensing: Achievements and challenges, *Remote Sens. Environ.*, 241, 111716,
804 doi:<https://doi.org/10.1016/j.rse.2020.111716>, 2020.

805 Zavala-Araiza, D., Lyon, D., Alvarez, R. A., Palacios, V., Harriss, R., Lan, X., Talbot, R. and Hamburg, S. P.: Toward a
806 Functional Definition of Methane Super-Emitters: Application to Natural Gas Production Sites, *Environ. Sci. Technol.*,
807 49(13), 8167–8174, doi:10.1021/acs.est.5b00133, 2015.

808 Zavala-Araiza, D., Alvarez, R. A., Lyon, D. R., Allen, D. T., Marchese, A. J., Zimmerle, D. J. and Hamburg, S. P.: Super-
809 emitters in natural gas infrastructure are caused by abnormal process conditions, *Nat. Commun.*, 8(1), 14012,
810 doi:10.1038/ncomms14012, 2017.

811 Zhang, M., Li, W. and Du, Q.: Diverse Region-Based CNN for Hyperspectral Image Classification, *IEEE Trans. Image*
812 *Process.*, 27(6), 2623–2634, doi:10.1109/TIP.2018.2809606, 2018.

813

814